AGU PUBLICATIONS

Water Resources Research

RESEARCH ARTICLE

10.1002/2017WR020754

Key Points:
- An observational gap in intermediate residence time scales of weeks to months could be closed through the novel ^{37}Ar tracer method
- Multitracer studies combined with numerical flow models are ideal tools to quantify mixing in surface water-groundwater systems
- We provide the first integration of tracer data covering all relevant time scales with a physically based numerical model

Supporting Information:
- Supporting Information S1
- Data Set S1

Correspondence to:
O. S. Schilling,
oliver.schilling.1@ulaval.ca

Citation:
Schilling, O. S., Gerber, C., Partington, D. J., Purtschert, R., Brennwald, M. S., Kipfer, R., . . . Brunner, P. (2017). Advancing physically-based flow simulations of alluvial systems through atmospheric noble gases and the novel ^{37}Ar tracer method. *Water Resources Research*, *53*. https://doi.org/10.1002/2017WR020754

Received 14 MAR 2017
Accepted 27 OCT 2017
Accepted article online 3 NOV 2017

Advancing Physically-Based Flow Simulations of Alluvial Systems Through Atmospheric Noble Gases and the Novel ^{37}Ar Tracer Method

Oliver S. Schilling[1,2], Christoph Gerber[3,4], Daniel J. Partington[5], Roland Purtschert[3], Matthias S. Brennwald[6], Rolf Kipfer[6,7,8], Daniel Hunkeler[1], and Philip Brunner[1]

[1]Centre for Hydrogeology and Geothermics (CHYN), University of Neuchâtel, Neuchâtel, Switzerland, [2]Now at Department of Geology and Geological Engineering, Université Laval, Pavillon Adrien-Pouliot, Québec, QC, Canada, [3]Climate and Environmental Physics and Oeschger Center for Climate Change Research, University of Bern, Bern, Switzerland, [4]Now at Land and Water, Commonwealth Scientific and Industrial Research Organisation (CSIRO), Glen Osmond, SA, Australia, [5]National Centre for Groundwater Research and Training, School of the Environment, Flinders University, Adelaide, SA, Australia, [6]Department of Water Resources and Drinking Water, Swiss Federal Institute of Aquatic Science and Technology (eawag), Dübendorf, Switzerland, [7]Institute of Biogeochemistry and Pollutant Dynamics, Swiss Federal Institute of Technology (ETH), Zürich, Switzerland, [8]Institute of Geochemistry and Petrology, Swiss Federal Institute of Technology, Zürich, Switzerland

Abstract To provide a sound understanding of the sources, pathways, and residence times of groundwater water in alluvial river-aquifer systems, a combined multitracer and modeling experiment was carried out in an important alluvial drinking water wellfield in Switzerland. ^{222}Rn, ^{3}H/^{3}He, atmospheric noble gases, and the novel ^{37}Ar-method were used to quantify residence times and mixing ratios of water from different sources. With a half-life of 35.1 days, ^{37}Ar allowed to successfully close a critical observational time gap between ^{222}Rn and ^{3}H/^{3}He for residence times of weeks to months. Covering the entire range of residence times of groundwater in alluvial systems revealed that, to quantify the fractions of water from different sources in such systems, atmospheric noble gases and helium isotopes are tracers suited for end-member mixing analysis. A comparison between the tracer-based mixing ratios and mixing ratios simulated with a fully-integrated, physically-based flow model showed that models, which are only calibrated against hydraulic heads, cannot reliably reproduce mixing ratios or residence times of alluvial river-aquifer systems. However, the tracer-based mixing ratios allowed the identification of an appropriate flow model parametrization. Consequently, for alluvial systems, we recommend the combination of multitracer studies that cover all relevant residence times with fully-coupled, physically-based flow modeling to better characterize the complex interactions of river-aquifer systems.

1. Introduction

The interactions between surface water (SW) and groundwater (GW) in alluvial valleys can be extremely dynamic and complex (Huggenberger et al., 1998; Partington et al., 2017; Sophocleus, 2002; Winter et al., 1998). Physically-based flow models such as MODFLOW (Harbaugh, 2005), FEFLOW (Dirsch, 2014), HydroGeoSphere (Therrien et al., 2010), and ParFlow (Kollet & Maxwell, 2006) are typically used for the simulation of such SW-GW systems (Anderson et al., 2015) and as prediction tools for alluvial drinking water stations (e.g., Bauser et al., 2010; Hendricks Franssen et al., 2011; Kurtz, et al., 2013). In general practice, only hydraulic heads and SW discharge are used for the calibration of SW-GW models (e.g., Anderson et al., 2015; Simmons et al., 2012). However, hydraulic heads alone do not contain sufficient information to simultaneously reproduce GW levels, exchange fluxes, mixing ratios, and residence times. Hydraulic conductivity (K) and porosity (n) of the aquifer (K_{aq} and n_{aq}) are strongly correlated toward a transient reproduction of fluxes, and through observations of hydraulic heads alone only the ratio between the two variables can be identified (e.g., Delottier et al., 2016; Townley, 2012). Moreover, even though the hydraulic conductivity of the riverbed (K_{rb}) is a first-order control for exchange fluxes between SW and GW (Boano et al., 2014; Mattle et al., 2001), K_{rb} is often poorly characterized. K_{rb} is often insensitive to hydraulic heads because alluvial valleys are typically characterized by large aquifer cross sections but small rivers that flow across these aquifers. Consequently, numerical models of SW-GW systems are often underinformed and structurally flawed (Bredehoeft, 2005; Simmons et al., 2012).

To improve the structure and calibration of SW-GW models, a variety of additional measurements of SW-GW systems can be considered (e.g., Brunner et al., 2017): Measurements of fluxes, of GW residence times and of the sources of pumped GW, for example, provide important information about alluvial SW-GW systems (Anderson et al., 2015; Simmons et al., 2012). While residence times are not straightforward to use in the context of flow model calibration (e.g., McCallum et al., 2014a, 2014b), end-member mixing ratios, for example, between older GW and recently infiltrated SW (e.g., McCallum et al., 2010), could be a promising alternative to inform complex SW-GW models.

In the last two decades, measurements of environmental tracers have been widely and successfully used to estimate recharge locations, recharge temperatures, and the residence times of GW on a large range of temporal and spatial scales. Multitracer studies, where tracers with different properties and with different measurement time scales are combined, have proven to be highly suited for the characterization of complex GW systems (Åkesson et al., 2015; Althaus et al., 2009; Gardner et al., 2011; Gerber et al., 2017; Mayer et al., 2014; McCallum et al., 2014a, 2014b) Most importantly, through the application of multiple tracers, the tracers which are best suited for an end-member mixing analysis of the given system can be identified (Cook & Böhlke, 2000; Harvey & Gooseff, 2015; Kipfer et al., 2002; Purtschert, 2008). Multiple studies demonstrated how information concerning the mixing ratio of water from different sources can be obtained, including, but not restricted to, the following tracers: electrical conductivity (e.g., Vogt et al., 2010), inorganic ions (e.g., Herczeg & Edmunds, 2000), stable water isotopes (e.g., Bertrand et al., 2010), atmospheric noble gases (e.g., Solomon et al., 2010), CFCs (e.g., Bourke et al., 2015), or $^{3}H/^{3}He$ (e.g., Beyerle et al., 1999). In order to reliably estimate mixing between different types of end-members (e.g., recently infiltrated SW and old GW), the physicochemical behavior of the tracer, the local residence time scales, and the composition of the different end-members that are present in the system, need to be known.

Despite many different environmental tracer methods being available, a critical temporal gap in the coverage of residence times can be identified: there is a gap between the short-lived radioactive tracer ^{222}Rn (half-life = 3.82 days), which is suited for very short measurement time scales from days to 2 weeks, and the other available tracer methods, which are suited for time scales of multiple months to millennia. The intermediate time scale from 2 weeks to a few months, however, is often the most relevant for a robust characterization of residence times in alluvial SW-GW systems. The rare radioactive tracer argon-37 (^{37}Ar) has the potential to bridge this gap: it is measurable at natural levels and has a half-life of 35.1 days, ideal for informing the intermediate time scales between ^{222}Rn and $^{3}H/^{3}He$ (Loosli et al., 2000; Riedmann & Purtschert, 2011). While the ^{37}Ar concentration in the atmosphere is very low, neutron-induced and muon-induced nuclear reactions produce ^{37}Ar in soil gas and GW (Riedmann & Purtschert, 2011), where it accumulates and can potentially be used for dating in a similar way as ^{222}Rn. The intermediate time scale of weeks to months could therefore potentially be covered by ^{37}Ar.

In this paper, we close the temporal observation gap by introducing the novel ^{37}Ar tracer to inform on intermediate residence time scales from 2 weeks to multiple months. We demonstrate the potential of this new tracer by combining it with other tracers and a physically-based model simulating the sources and residence times of GW in an alluvial drinking water wellfield. The interpretation of ^{37}Ar requires some basic information on the flow field, which is also established with the flow model. The novelty of the contribution lies not only in the introduction of a new tracer but also in the integration of an end-member mixing analysis enabled through ^{37}Ar in a fully-coupled, physically-based numerical model. Except for a few rare cases such as Carniato et al. (2015), Delsmann et al. (2016) and Hunt et al. (2006), only simple 1-D or lumped parameter models have been used in combination with multitracer studies. Such simplistic models, however, are strongly limited for the analysis of complex SW-GW exchange fluxes compared to the complete analyses facilitated by physically-based flow models (see Turnadge & Smerdon, 2014). Our model simulates a unique transient pumping experiment where the abstraction through a large wellfield is reduced significantly and introduces a known transient forcing to the system. To carry out this experiment, the drinking water supply of the city of Bern had to be reorganized temporarily. This combination of multiple tracers with a physically-based model provides a quantitative basis to discuss the potential of ^{37}Ar.

2. Materials and Methods

We first provide the theory for a number of environmental tracers and introduce the field site. For the integration of the information obtained through the different tracers, a numerical flow model of an alluvial

drinking water wellfield was then matched against observations of hydraulic heads. Subsequently, multiple scenarios of K_{rb} and n_{aq}, which all fit the hydraulic head observations equally well, were tested and compared to travel times of infiltrated SW and the mixing ratio between SW and GW that is pumped by the drinking water wells. These simulations were subsequently compared to environmental tracer-based estimates of travel times and mixing ratios. For this purpose, ^{222}Rn, ^{3}H/^{3}He, and atmospheric noble gases were measured alongside the new ^{37}Ar tracer method to quantify the flow dynamics and mixing ratios in the alluvial SW-GW system. The multitracer study was carried out during a controlled transient manipulation to an important alluvial drinking water wellfield in Switzerland, which provided optimal conditions for analyzing how the tracer measurements reflect system transience.

2.1. Theory of Natural Environmental Tracer Methods

2.1.1. The ^{222}Rn Dating Method

The radioactive isotope ^{222}Rn with a half-life ($T_{1/2}$) of 3.82 days is produced in the soil via the decay-chain of ^{238}U. The gradual accumulation of ^{222}Rn in GW can be used as a tracer for residence times and was first demonstrated by Hoehn and von Gunten (1989). It is now considered as an established method to estimate SW-GW exchange fluxes (e.g., Bourke et al., 2014; Cecil & Green, 2000; Cranswick et al., 2014; Harvey & Gooseff, 2015; Vogt et al., 2010). According to Vogt et al. (2010), the ingrowth of ^{222}Rn in GW can be described by the following equation:

$$AC_{222_{Rn}}(t) = AC_{222_{Rn,eq}}\left(1 - e^{-\lambda_{222_{Rn}} t}\right) + AC_{222_{Rn,SW}} \cdot e^{-\lambda_{222_{Rn}} t} \quad (1)$$

with t representing time. $\lambda_{222_{Rn}}$ is the decay constant (0.182 days^{-1}), $AC_{222_{Rn,eq}}$ the activity concentration of ^{222}Rn at secular equilibrium, $AC_{222_{Rn}}(t)$ the activity concentration at time t, and $AC_{222_{Rn,SW}}$ the activity concentration of SW at the time of infiltration (typically close to 0). The ^{222}Rn-based residence time (also "apparent age") of GW can be estimated by solving equation (1) for t:

$$t_{222_{Rn}} = {\lambda_{222_{Rn}}}^{-1} \cdot \ln\left(\frac{AC_{222_{Rn,eq}} - AC_{222_{Rn,SW}}}{AC_{222_{Rn,eq}} - AC_{222_{Rn}}(t)}\right) \quad (2)$$

After approximately three half-lives of ^{222}Rn, residence times cannot be further differentiated based on ^{222}Rn measurements, as the activity concentration becomes indistinguishable from the equilibrium activity concentration within the measurement uncertainty (e.g., Cecil & Green, 2000).

2.1.2. The ^{37}Ar Dating Method

^{37}Ar with a $T_{1/2} = 35.1$ days is a very rare, radioactive isotope of argon (Loosli et al., 2000; Loosli & Purtschert, 2005). Like ^{222}Rn, ^{37}Ar is only produced in the subsurface in significant quantities. At shallow depths of up to 10 m, activation of Ca by cosmic neutrons is the dominant reaction channel (40Ca(n, α)^{37}Ar; Fabryka-Martin, 1988). At greater depths, the muon capture reactions ^{39}K(μ^-,2n)^{37}Ar and ^{40}K(μ^-,3n)^{37}Ar become increasingly dominant (Fabryka-Martin, 1988; Johnson et al., 2015; Riedmann & Purtschert, 2011, 2016). Both pathways lead to an exponentially decreasing production rate of ^{37}Ar with depth, which is characterized by the attenuation length ℓ (L). ℓ depends mainly on the bulk density of the sediments (including water and soil gas; Guillon et al., 2016). In case of predominantly horizontal GW flow and full saturation of the porous media, advective and diffusive vertical transport is negligible and the exponential production profile is maintained in the ^{37}Ar activity concentration of GW. ^{37}Ar activity concentrations are measured in mBq/L_{Ar} and converted to mBq/L_{water} by using the concentration of dissolved Ar in the GW (Riedmann & Purtschert, 2011).

At secular equilibrium, the ^{37}Ar activity concentration as a function of depth d can be expressed by

$$AC_{37_{Ar,eq}}(d) = AC_{37_{Ar,eq}}(0) \cdot e^{-d/\ell} \quad (3)$$

where $AC_{37_{Ar,eq}}(0)$ is the hypothetical activity concentration at $d = 0$ m.

If this secular equilibrium activity concentration profile is known, ^{37}Ar can be used as a dating tool on time scales of weeks to months for SW that freshly infiltrated into an aquifer, as the ^{37}Ar activity concentration in GW is approaching the secular equilibrium activity concentration:

$$AC_{37_{Ar}}(d,t) = AC_{37_{Ar,eq}}(d) \cdot \left(1 - e^{-\lambda_{37_{Ar}} t}\right) + AC_{37_{Ar,SW}} \cdot e^{-\lambda_{37_{Ar}} t} \quad (4)$$

$AC_{37_{Ar,SW}}$ is the activity concentration of SW at the time of infiltration (typically close to 0). The decay constant $\lambda_{37_{Ar}}$ is 0.0197 day^{-1}. Similarly to ^{222}Rn, the ^{37}Ar residence time is obtained by the ingrowth from the initial activity $AC_{37_{Ar,SW}}$ to the equilibrium profile. As for ^{222}Rn, after about three half-lives of ^{37}Ar (approximately 110 days), the activity concentration of ^{37}Ar becomes indistinguishable from the secular equilibrium activity concentration within the ^{37}Ar measurement uncertainty. This makes ^{37}Ar an ideal tracer for intermediate time scales of weeks to months. The ^{37}Ar residence time is given by

$$t_{37_{Ar}} = \lambda_{37_{Ar}}{}^{-1} \cdot \ln\left(\frac{AC_{37_{Ar,eq}}(d) - AC_{37_{Ar,SW}}}{AC_{37_{Ar,eq}}(d) - AC_{37_{Ar}}(d,t)}\right) \quad (5)$$

This calculation of ^{37}Ar residence times is based on two simplifying assumptions: First, it is assumed that the GW approximately remains at the same depth, i.e., that flow is approximately horizontal. This requires the elaboration of a flow model. Second, the aquifer is assumed to be homogeneous with respect to porosity and elemental composition. If the sampling well is screened over several meters, the depth where the equilibrium concentration is equal to the expected equilibrium concentration for the mixed sample is calculated with

$$d_m = d_u + \ell \cdot \left(\ln\left((d_l - d_u)/\ell\right) - \ln\left(1 - e^{-(d_l - d_u)/\ell}\right)\right) \quad (6)$$

where d_u and d_l are upper and lower limits of the screen, respectively.

The ^{37}Ar-dating concept is illustrated in Figure 1 for a hypothetical parcel of SW with a typical near-zero $AC_{37_{Ar,SW}}$ of 5×10^{-5} mBq/L_{water} (Riedmann, 2011): the SW parcel infiltrates rapidly into the subsurface, down to a depth of 10 m. At a depth of 10 m, the water parcel starts to move horizontally, following the predominant direction of GW flow. The secular equilibrium depth profile of ^{37}Ar can be quantified with equation (3). For example, with a hypothetical attenuation length ℓ of 15.9 m the secular equilibrium at a depth of 10 m is 0.00268 mBq/L_{water}. If plotted as in Figure 1, equation (4) can be used to draw isolines of

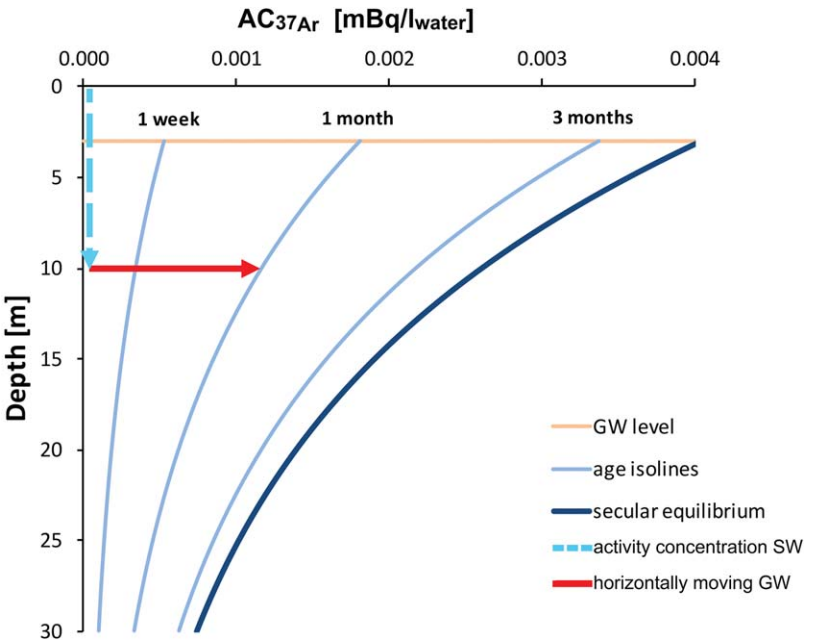

Figure 1. ^{37}Ar-dating concept. The concept is illustrated for a parcel of SW with a near-zero $AC_{37_{Ar,SW}}$ that infiltrated rapidly, and which starts moving horizontally in GW at a depth of 10 m. Once in the subsurface, the water parcel starts accumulating ^{37}Ar. After 110 days, the water parcel reaches the secular equilibrium of ^{37}Ar, which, at 10 m depth ($AC_{37_{Ar,eq}}$ (10 m), would be 0.00268 mBq/L_{water} for an attenuation length of 15.9 m. If the water parcel is sampled before 110 days of residing in the subsurface, for example, after 1 month, the ^{37}Ar activity concentration can be used to identify the residence time of that water parcel.

different residence times, e.g., for 1 week, 1 month, and 3 months. After a residence time of 1.9 days, the accumulated ^{37}Ar exceeds the initial amount ^{37}Ar of atmospheric origin in the water, and after 8.5 days the initial ^{37}Ar present in the infiltrating water parcel accounts for less than 10% of total ^{37}Ar. If the water parcel is sampled within less than 110 days after infiltration, $AC_{37_{Ar}}(d,t)$ can be used to determine the water parcel's residence time in the subsurface using equation (5). After 110 days of residing in the subsurface, however, the water parcel approaches the secular equilibrium such that it becomes indistinguishable from $AC_{37_{Ar,eq}}$ (10 m) with the current detection limits.

2.1.3. The ^{3}H/^{3}He Dating Method

Tritium (^{3}H) is the radioactive isotope of hydrogen that decays to ^{3}He with a half-life of approximately 4,500 days. It is naturally present in the Earth's atmosphere and primarily produced through cosmic-rays-induced decay of atmospheric nitrogen (Lucas & Unterweger, 2000; Solomon & Cook, 2000). ^{3}H concentrations are expressed in tritium units (TU), and the natural background concentration of ^{3}H in the atmosphere is between 1 and 6 TU (Solomon & Cook, 2000). In the well-established ^{3}H/^{3}He method, the apparent age of GW is estimated by comparing the measured concentration of ^{3}H in GW to the tritiogenic portion of the measured ^{3}He (e.g., Beyerle et al., 1999; Kipfer et al., 2002; Schlosser et al., 1988; Solomon & Cook, 2000). While the tritiogenic portion of ^{3}He (denoted as ^{3}He*) cannot be directly measured, ^{3}He* can be estimated based on noble gas measurements (e.g., Kipfer et al., 2002; Solomon & Cook, 2000). The apparent ^{3}H/^{3}He water age, or ^{3}H/^{3}He residence time of GW, is defined as

$$t_{^3\mathrm{H}/^3\mathrm{He}} = {\lambda_{^3\mathrm{H}}}^{-1} \cdot \ln\left(\frac{^3\mathrm{He}^*}{^3\mathrm{H}} + 1\right) \tag{7}$$

$\lambda_{^3\mathrm{H}}$ is the decay constant of ^{3}H (1.54×10^{-4} days^{-1}). The ^{3}H/^{3}He method allows identifying residence times of approximately 2 months to 50 years (Harvey & Gooseff, 2015).

2.1.4. Analysis of Atmospheric Noble Gases

2.1.4.1. End-Member Mixing Analysis Based on Noble Gas Recharge Temperatures

The equilibrium solubility of the stable atmospheric noble gases He, Ne, Ar, Kr, and Xe can be used to estimate the water temperature during the moment of recharge (Aeschbach-Hertig & Solomon, 2013; Kipfer et al., 2002). This recharge temperature is commonly known as the noble gas recharge temperature (NGRT). The NGRT in turn allows estimating the time of recharge if the temperature chronicle in the recharge area is known. To calculate the NGRT from stable atmospheric noble gas concentrations, the Closed Equilibrium (CE) model was used in this study (Aeschbach-Hertig et al., 1999; Aeschbach-Hertig & Solomon, 2013; Kipfer et al., 2002).

If, in a given SW-GW system, there are GW components that have residence times of at least 1 year and, during this long residence time, have become relatively well mixed, the NGRT of that GW component ($\mathrm{NGRT}_{\mathrm{GW,old}}$) will reflect the average annual air temperature in the recharge area. The NGRT of freshly infiltrated SW ($\mathrm{NGRT}_{\mathrm{SW}}$), on the other hand, still maintains the signal of the air temperature at the time of infiltration. In a system where these two components are present, the NGRT can be used to infer mixing if the approximate recharge temperature of the freshly infiltrated SW can be determined through a residence time analysis. While NGRT do not mix linearly (Aeschbach-Hertig & Solomon, 2013; Kipfer et al., 2002), for the small NGRT variation encountered in this study, NGRT mixing can reasonably be approximated by the following linear mixing equation:

$$\mathrm{NGRT}_{\mathrm{GW}}(t) = x \cdot \mathrm{NGRT}_{\mathrm{GW,old}} + (1-x) \cdot \mathrm{NGRT}_{\mathrm{SW}}(t) \tag{8}$$

2.1.4.2. End-Member Mixing Analysis Based on the ^{3}He/^{4}He Isotopic Ratio

The isotopic ratio of ^{3}He/^{4}He in GW can also be used as an indicator of two-component mixtures and residence times (Solomon, 2000). The atmospheric ratio of ^{3}He/^{4}He is 1.384×10^{-6}, and 1.36×10^{-6} in air-equilibrated water (AEW). Multiple processes significantly alter this ^{3}He/^{4}He ratio in shallow GW: (a) terrigenic production of mainly ^{4}He and (b) tritiogenic production of ^{3}He. If the estimated amount of tritiogenic ^{3}He (estimated as described in section 2.1.3) is subtracted from the measured ^{3}He, the resulting $^3\mathrm{He}_{\mathrm{corr}}/^4$He ratio then only represents the atmospheric and terrigenic components of ^{3}He and ^{4}He. Because neither $^3\mathrm{He}_{\mathrm{corr}}$ nor ^{4}He are produced in significant amounts on the short time scales that are relevant for drinking water safety (days to months), $^3\mathrm{He}_{\mathrm{corr}}/^4$He on that time scale can only change due to the mixing of water with different $^3\mathrm{He}_{\mathrm{corr}}/^4$He ratios. The $^3\mathrm{He}_{\mathrm{corr}}/^4$He ratio can therefore be used to analyze mixing between a freshly infiltrated SW component with a $^3\mathrm{He}_{\mathrm{corr}}/^4$He ratio corresponding to the AEW ratio (1.36×10^{-6})

$\left(\frac{^3He_{corr}}{^4He}(SW)\right)$ and an older GW component with accumulated ^4He resulting in a significantly lower $^3He_{corr}/^4He$ ratio $\left(\frac{^3He_{corr}}{^4He}(GW)\right)$; Kipfer et al., 2002):

$$\frac{^3He_{corr}}{^4He}(t) = x \cdot \frac{^3He_{corr}}{^4He}(GW) + (1-x) \cdot \frac{^3He_{corr}}{^4He}(SW) \quad (9)$$

2.2. Study Site

2.2.1. Hydrology, Hydrogeology, and Climate

The Upper Emme valley is a typical pre-alpine, alluvial catchment situated on the northern border of the Swiss Alps (see Figure 2). The valley bottoms in the lower part of the catchment consist of coarse, quaternary alluvial sandy gravel (80% gravel and 20% sand), forming a highly conductive unconfined aquifer (Blau & Muchenberger, 1997). The catchment is spread over an altitude of 673–2221 m asl and covers an area of 194 km^2, which is drained by two rivers, the Emme River and the Roethebach tributary, with an average discharge of 4.4 and 0.7 m^3/s, respectively. These rivers are extremely dynamic and provide the main source of recharge to the alluvial aquifer of the Upper Emme valley (Blau & Muchenberger, 1997; Käser & Hunkeler, 2015). The lowest part of the catchment consists of the main Emme River valley with an average topographic gradient of 0.9% (Käser & Hunkeler, 2015). Approximately 8 km upstream of the outlet, the tributary enters the main valley. The whole aquifer, which extends into the tributary valley, spans an approximate area of 6 km^2 (Käser & Hunkeler, 2015). In the area of the studied aquifer, the valley has a width of 200–400 m. The aquifer is limited underneath by impermeable sediments of the freshwater molasses. The aquifer serves as an important drinking water resource and provides 45% of the drinking water consumed in the region of the Swiss capital Bern (Biaggi et al., 2005). The wellfield is situated on the Ramsei Plain, toward the outlet of the valley (see close-up in Figure 2). GW is pumped in roughly equal parts from eight (single-depth) suction wells spaced at approximately 100 m and aligned in parallel to the river. The distance between the drinking water wells and the Emme River is 300 m toward the river bend marking the upstream end of the Ramsei Plain, and 125 m parallel to the wells. Water is pumped from a depth of 10 m in the three upstream wells, and from a depth of 15 m in the five downstream wells. In total, the drinking water station pumps 0.4 m^3/s of GW. This GW abstraction is substantial relative to the total water balance of the system: it can amount to up to 50% of the total outflow of SW and GW out of the valley (Käser & Hunkeler, 2015; Würsten, 1991). The aquifer around the Ramsei Plain has an average thickness of 25 m (Würsten, 1991). The maximum vertical extent of the aquifer at the Ramsei Plain is 46 m. Two pumping tests at the locations of A24 and A26 (see Figure 2) revealed average aquifer hydraulic conductivities (K_{aq}) between 200 and 500 m/d, with maximal values of more than 1,350 m/d (Würsten, 1991). The hydraulic conductivity of the riverbed (K_{rb}) and the porosity of the aquifer (n_{aq}) have not been systematically measured, but based on their pumping test data, Würsten (1991) and Blau and Muchenberger (1997) assumed n_{aq} values between 0.1 and 0.3.

At the drinking water station, the average annual precipitation is 1,300 mm, the potential evapotranspiration 550 mm, and the average annual air temperature is 8°C (Figura et al., 2011, 2013, 2015; Käser & Hunkeler, 2015; Würsten, 1991). In very dry summers and very cold winters, segments of the Emme River may run completely dry (Würsten, 1991). Käser and Hunkeler (2015) measured the water temperature and electrical conductivity in the SW directly above the riverbed near the drinking water wellfield, and identified alternating locations of losing and gaining conditions, indicating that there is a complex pattern of interactions between SW and GW.

2.2.2. Measurement Network

A dense measurement network for the observation of a multitude of hydrological and climatic variables covers the entire alluvial valley (Käser & Hunkeler, 2015; Kropf et al., 2014; Lapin et al., 2014). SW discharge is continuously monitored at a 10 min interval at four river gauging stations, with one station located at the outlet of the catchment 1.5 km downstream of the wellfield, and two stations measuring the inflow from the Emme River and the tributary into the main valley, 5.5 km upstream of the wellfield. GW levels are continuously recorded at 10–15 min intervals in more than 30 piezometers. Fourteen of these piezometers are located in the immediate proximity of the drinking water wellfield (see close-up of Figure 2). These piezometers are screened in the upper 10–15 m of the soil. A strategic multilevel piezometer (A41) located immediately upstream of the drinking water wellfield, just across the river, was installed to allow sampling of water

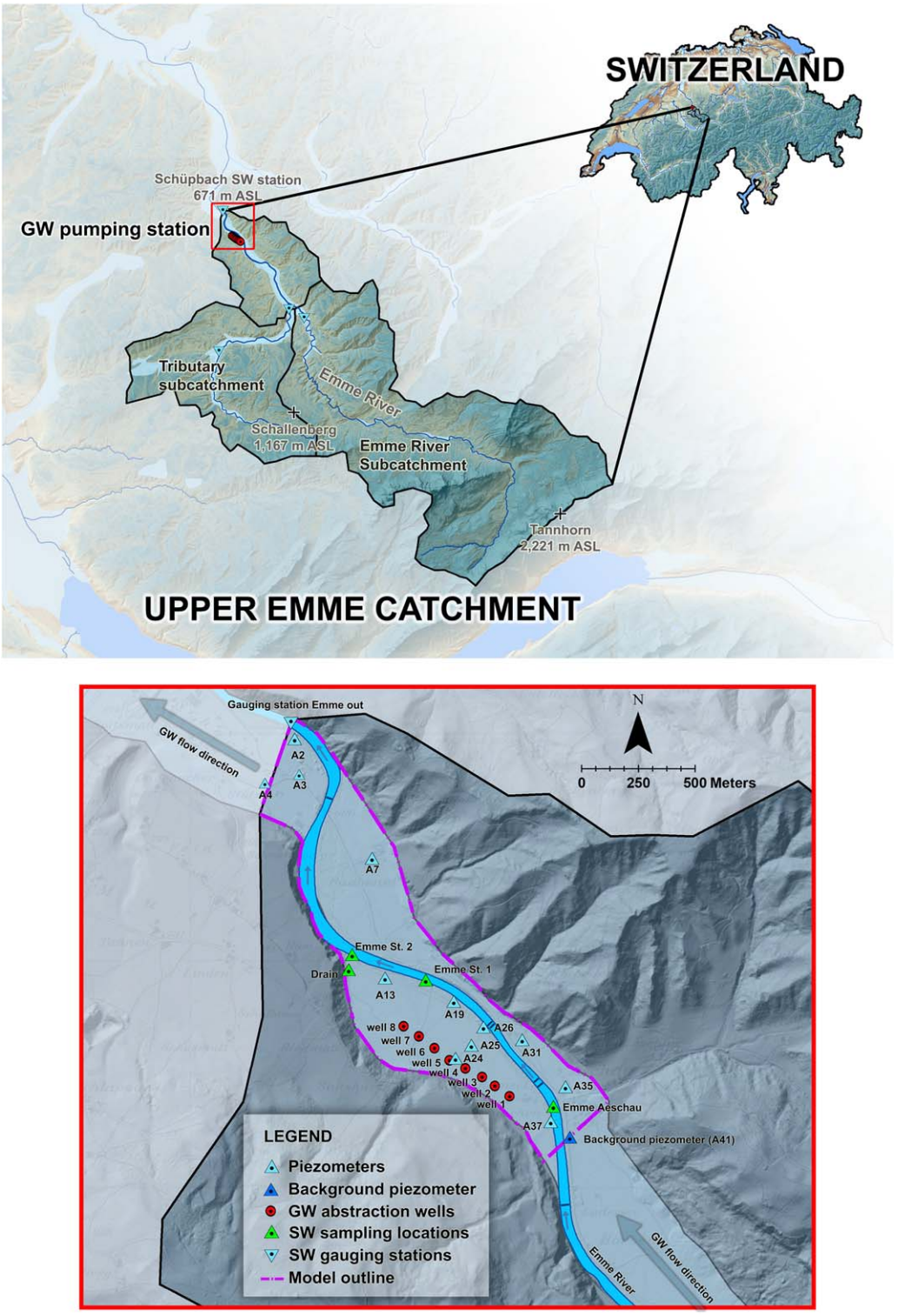

Figure 2. (top) Maps of the Upper Emme catchment and (bottom) a close-up of the GW pumping station on the Ramsei Plain in the lower part of the catchment. In the top image, bright blue colors in the valley bottoms indicate aquifers. The different subcatchments are separated by solid black lines. The three gauging stations that measure the discharge of each subcatchment are indicated by inverted blue triangles.

also at higher depths than the other piezometers and the drinking water wells. The screened depths are 0–10, 11.5–13.5, 16–18, and 21.5–23.5 m.

2.3. Controlled Pumping Experiment and Multitracer Sampling

For the multitracer experiment, a large-scale and controlled forcing to the study site was introduced through a transient pumping experiment that was implemented in collaboration with the water authorities of Bern (WVRB). The controlled forcing was expected to produce (i) altered SW-GW interactions and (ii) a change in the sources of the pumped water. During the 12 months prior to the multitracer experiment, the average abstraction rate at the drinking water station was constant at 360 L/s (herein referred to as the *maximum* or *max* pumping regime). This long period of maximal abstraction resulted in a hydraulic quasi steady state. A transient manipulation to this hydraulic quasi steady state was achieved through a reduction of the pumped GW by 40% for the period of 1 week. The aim was to create reduced hydraulic gradients and approach a new hydraulic quasi steady state. For 7 days, from 26 January 2015 14:00 until 2 February 2015 14:00, the pumping rate was reduced to the smallest technically possible rate of 225 L/s (herein referred to as the *minimum* or *min* pumping regime). The experiment took place during a sustained low flow period at the end of January 2015. During these winter periods, precipitation mainly falls as snow and SW discharge is mainly affected by SW-GW interactions, which allows for optimal detection of the SW-GW dynamics.

The average SW discharge during the 7 days of reduced pumping was 1.4 m^3/s at the closest upstream gauging station and 2.3 m^3/s at the downstream gauging station of the Emme River. The average air temperature was 3.3°C. Precipitation amounted to a total of 32.9 mm but was retained as snow on the floodplain and overland flow or infiltration on the floodplain were negligible. To investigate the changes of SW-GW exchange rates, the pumping experiment was accompanied by SW dilution gauging tests at two locations close to the wellfield (upstream: Emme St. 1, downstream: Emme St. 2, see close-up in Figure 2). The dilution tests were carried out using fluorescein and the GGUN-FL30 flow-through field fluorometers (Schnegg, 2003).

In addition to continuous hydraulic and meteorological measurements, water samples were taken for analysis of the chemical composition and of different natural environmental tracers (^{222}Rn, ^{37}Ar, ^{3}H/^{3}He, and atmospheric noble gases) immediately before, during, and after the pumping experiment. The samples were taken at discrete locations in the river, in piezometers A13, A25, A26, A41, as well as in the pumping wells 1, 5, and 7. The GW in the multilevel piezometer A41 is assumed to represent the background end-member, i.e., the oldest possible GW in the studied domain, and was used to obtain depth profiles of ^{222}Rn and ^{37}Ar. The solid state alpha detector RAD7 (DURRIDGE, 2014) was used in conjunction with the RAD H2O accessory (DURRIDGE, 2012) to measure the activity concentration of ^{222}Rn in water. ^{222}Rn was sampled in 250 mL glass vials and analyzed in a closed-loop gas analysis for four 5 min counting intervals as described by Vogt et al. (2010). ^{37}Ar was measured in the Low Level Counting Laboratory of the University of Bern in Switzerland (Loosli & Purtschert, 2005). To measure the activity of ^{37}Ar, 2–3 t of water per sample were degassed directly in the field in order to extract sufficient amounts of ^{37}Ar for subsequent laboratory analysis (Purtschert et al., 2013). From the extracted gas, Ar was separated by preparative gas chromatography (Riedmann & Purtschert, 2016) and then measured by low level counting (Riedmann, 2011). Noble gas concentrations, He isotopes and ^{3}H were analyzed at the Noble Gas Mass Spectrometry Laboratory of the Swiss Federal Institute of Technology in Zurich, Switzerland, using standard measuring protocols (Beyerle et al., 2000).

2.4. Surface Water-Groundwater Modeling

2.4.1. Modeling Strategy

To (1) identify the dominant flow directions, which is required for the interpretation of the ^{37}Ar tracer results, and (2) to correctly predict the mixing ratios between older GW and SW that infiltrated only days to a few weeks ago, which is required for the management of the drinking water station, both SW and GW flow were explicitly simulated in a physically-based and fully-integrated way, and the movement of water was tracked throughout the entire modeling domain. Using a fully-integrated SW-GW flow model allows a dynamic simulation of SW-GW exchange fluxes without the need to predefine a priori unknown exchange flux locations and magnitudes. The choice for a fully-coupled model is also motivated by the fact that the

river is highly dynamic and changes its infiltrating regime from gaining to losing within very short distances.

The system was simulated using steady state and transient models. Using both approaches allowed analyzing the short-term reactions of the mixing ratios and travel times to a change in pumping as well as the long-term reaction when the system reaches steady state. Steady state simulations were carried out for the *maximum* pumping regime and for the *minimum* pumping regime. Transient simulations were carried out for the duration of the pumping experiment, with the steady state results of the *maximum* regime used as initial conditions. Specifically, the steady state simulations correspond to (1) the *maximum* pumping regime with measured hydraulic forcings from 21 January 2015 00:00 and (2) the *minimum* pumping regime with measured forcings from 2 February 2015 00:00. The transient simulations covered the entire duration of the pumping experiment and consisted of hourly changing boundary conditions. The transient simulations started off the *maximum* steady state (i.e., 21 January 2015 00:00), and finished 4 days after the end of pumping experiment, on 6 February 2015 23:59.

All simulations were analyzed for the sources of the pumped water and for travel times. To quantify the mixing ratio between the different sources, the pumped water was separated into the relative amounts of water that entered the model through the GW boundary conditions versus water that entered the model through the SW boundary conditions. The mean travel time of the pumped SW component between the river and the wells was defined as the time required until the SW component has reached 50% of its steady state value in the pumped water. Mixing ratio and travel time analyses were carried out for (1) the *maximum* steady state, (2) the transient state immediately before the end of the *minimum* pumping experiment on 2 February 2015 12:30 (from now on denoted as the state *trans*), and (3) the *minimum* steady state.

While the K_{aq} value used in all simulations resulted from a calibration against hydraulic head observations, to quantify the influence of (the unknown) K_{rb} and n_{aq} on the exchange fluxes and mixing ratios, multiple different scenarios of K_{rb} and n_{aq}, which all fit the hydraulic heads equally well, were tested. For all different scenarios of K_{rb} and n_{aq}, the three different simulated states *maximum*, *trans*, and *minimum* were compared to tracer measurements in order to identify an appropriate model among the different scenarios tested.

2.4.2. Model Setup

2.4.2.1. Numerical Simulator

For the flow simulations, the model HydroGeoSphere (HGS; Aquanty Inc, 2016; Brunner & Simmons, 2011; Kurtz et al., 2017; Therrien et al., 2010) was used. HGS uses the Richards equation and the van Genuchten parametrization to simulate unsaturated subsurface flow, and surface water flow is calculated using the diffusive-wave approximation of the Saint-Venant equations. HGS was chosen as it directly simulates all the relevant SW-GW processes in a fully-integrated way and has been demonstrated to be an ideal tool for the simulation of complex alluvial SW-GW systems with dynamic exchange flux patterns (e.g., Ala-Aho et al., 2017; Banks et al., 2011; Chow et al., 2016; Fleckenstein et al., 2006; Frei et al., 2010; Schilling et al., 2014; Tang et al., 2017).

As one objective of the flow simulations was to allow the comparison between tracer-based mixing ratios and simulated mixing ratios, we chose the Hydraulic Mixing-Cell flow tracking tool (HMC; Partington et al., 2011, 2012, 2013) to track the flow of water from different sources throughout the modeling domain. HMC utilizes the hydraulic flow solution of the HGS model, tags any inputs to the model domain as specified by the boundary conditions and then tracks the fraction of these inputs in each of the model cells. In contrast to particle tracking approaches, modified mixing cell approaches such as HMC allow obtaining transient mixing ratios of water from all different sources at every cell within the model without much extra computational cost and postprocessing. However, mixing cell approaches may introduce numerical dispersion if the mesh and the time step size are not optimally set (e.g., Harrington et al., 1999; Rao & Hathaway, 1989). Rao and Hathaway (1989) pointed out that if the mesh and time step size are optimal, numerical dispersion is minimized, and could even be controlled such that it approaches hydrodynamic dispersion. In this study, numerical dispersion was minimized by using a finely discretized numerical grid and a sub-time-stepping scheme that automatically calculates the optimal time step size (see Partington et al., 2011).

2.4.2.2. Model Setup

High-resolution topographical maps of the floodplain (swisstopo, 2010), the aquifer confining layer (AWA, 2016), and the riverbed were used to define the 3-D structure of the model. The riverbed topography was obtained for this study with through-water photogrammetric analysis (e.g., Feurer et al., 2008) of aerial

images taken with a drone on 20 March 2015 (resolution of 0.25 m). Following the guidelines of Käser et al. (2014) for mesh generation of alluvial systems, an approximately equilateral triangular mesh with an average side length of 17.5 m for the floodplain and 8.5 m for the river, resulting in 10,983 elements per layer, was generated with GridBuilder (McLaren, 2011). Vertically, the model consisted of 15 layers, covering the entire vertical aquifer extent: the top 5 layers covered 0.61% each, the next 4 layers 6.1%, and the last 5 layers 12%. At the location of the largest vertical extent (46 m) this resulted in layers of 0.28, 2.8, and 5.5 m thickness. The steady state solution was obtained by simulating 2,500 days with constant forcings. The Newton absolute and Newton residual convergence criteria were set to 10^{-5}.

2.4.2.3. Model Parametrization and Initial Calibration

The aquifer was conceptualized as a homogeneous sandy gravel aquifer with a van Genuchten α of 3.48 m^{-1}, a van Genuchten β of 1.75 and a S_{wr} of 0.05 (corresponding to values found for sandy gravel outwash by Li et al., 2008). Due to the limited number of pumping tests, K_{aq} was calibrated against observations of hydraulic heads measured in piezometers A4, A7, A19, A24, A25, A26, A31, A35, and A37 in an automated calibration of the *maximum* model using PEST (Doherty, 2015). A value of 550 m/d for K_{aq} was found to best reproduce the measurements. As values of the porosity of the aquifer (n_{aq}) were not available, and since n_{aq} is strongly correlated to K_{aq} toward reproducing flow (e.g., Anderson et al., 2015; Delottier et al., 2016; Townley, 2012), K_{aq} and n_{aq} cannot be simultaneously calibrated against hydraulic heads. Therefore, three different n_{aq} scenarios, which span typical values for sandy gravel aquifers documented in literature and are in accordance with the values suggested by previous field observations, were tested in combination with the calibrated K_{aq}: (i) a value of 0.43 (Li et al., 2008), (ii) a value of 0.2 (Fetter, 2001), and (iii) a value of 0.1 (Anderson et al., 2015).

The riverbed was conceptualized as a homogeneous sandy gravel layer with the same soil properties as the aquifer, but a fixed riverbed porosity (n_{rb}) of 0.41. As the water table next to the river is very close to the surface water level, no hydraulic disconnection between surface water and groundwater occurs (Lamontagne et al., 2014), and assuming homogeneous riverbed properties does therefore not introduce any bias in estimating exchange fluxes (Irvine et al., 2012; Schilling et al., 2017). It is also assumed that the hydraulic properties of the riverbed stay constant during the simulation. This is a reasonable assumption, as during the relatively short period of simulation no significant flood event occurred (see Gianni et al., 2016). The automatic calibration of K_{rb} alongside K_{aq} with the *maximum* model revealed that K_{rb}, within a range of approximately 0.24 and 24 m/d, does not significantly alter the simulated hydraulic heads. To quantify the influence of different K_{rb} on mixing ratios and residence times, multiple K_{rb}-scenarios were simulated: 0.24, 2.4, and 24 m/d. Due to the very rough surface of the riverbed, with a mix of boulders, rocks, gravel, sand, and vegetation, a high flow resistance was incorporated by a high value for Manning's n (1.7×10^{-6} $d/m^{1/3}$).

2.4.2.4. Boundary Conditions

For all simulations, precipitation was corrected for potential evapotranspiration, which was calculated based on solar radiation and temperature measurements after Spreafico and Weingartner (2005). This resulted in 0 mm/d for the *maximum* regime, and 5.7 mm/d for the *minimum* regime. For the transient simulations, hourly measurements of a nearby meteorological station were used. The upstream BC for GW was split into two first-type (specified head) BCs, one underneath the floodplain that corresponded to the values measured in the background piezometer A41 (*max*: 690.969 m asl and *min*: 691.167 m asl), and one underneath the river with the floodplain BC value + 1 m, which corresponds to approximately 0.1 m water depth in the river, ensuring connected and losing conditions in the upstream part of the model (corresponding to the observations made by Käser & Hunkeler, 2015).

A specified head BC with the measured value of piezometer A3 (*max*: 671.715 m asl and *min*: 671.728 m asl) was fixed on the downstream end of the model domain. The SW inflow on the upstream side of the model was conceptualized as a second-type (specified flux) BC that corresponds to the sum of the inflows of the Emme River and the tributary measured at the closest upstream gauging stations (*max*: 1.702 m^3/s and *min*: 1.425 m^3/s). A small creek entering the Emme River approximately 200 m downstream of the upstream BC was implemented as a specified flux BC on the river bank (the tributary discharge is *max*: 0.086 m^3/s and *min*: 0.0075 m^3/s). The SW outflow was implemented as a critical depth BC. The eight pumping wells were implemented as specified nodal flux BCs, each located at the corresponding abstraction depth of the respective well. The pumping rate of the abstraction station is controlled separately for wells 1–4 (4,230 m^3/d per well during *maximum* flow and 2,250 m^3/d per well during *minimum* flow) and wells 5–8 (3,430 m^3/d

per well during *maximum* flow and 2,630 m^3/d per well during *minimum* flow) and was adjusted accordingly. The values that were used for the BCs of the *transient* simulations are provided in Figure 3. All other boundaries of the model were conceptualized as impermeable boundaries.

3. Results

3.1. Controlled Forcing of the System Through the Pumping Experiment

The measured pumping rates, water temperatures, GW levels, and SW discharge at the different measurement locations are illustrated in Figure 3. The SW inflow of the Emme River and the tributary were relatively stable during the pumping experiment (26 January 2015 14:00 to 2 February 2015 14:00) and varied slightly around an average of 1.4 m^3/s. The SW outflow of the catchment averaged at 2.29 m^3/s during that period, indicating gaining conditions overall. More specifically, the dilution tests (not shown in the figure) carried out during the *maximum* pumping regime indicated strongly gaining conditions with an average increase in SW discharge between Emme St. 1 and Emme St. 2 of 30%. During the *minimum* pumping regime, the average increase of SW discharge between the two stations rose to 50%, indicating more exfiltration of GW into the river in reaction to reduced pumping.

The rise in SW discharge between Emme St.1 and Emme St. 2 is in agreement with the strongly altered hydraulic gradients: the GW levels changed dramatically and rapidly in response to a change of the pumping rate. The change in GW levels relative to the levels of 17 January 2015 00:00 is shown in Figure 3: GW levels rose by 1 m and more in the pumping wells, and up to 0.5 m in the sampled piezometers. The GW levels stabilized within a few days, and got lower as quickly as they rose after the end of the *minimum* pumping experiment. Even the GW levels in the background piezometer A41, approximately 350 m upstream of well 1 and on the far side of the Emme River reacted with a rise of approximately 0.4 m in response to a reduction in the pumping rates. Piezometers as far as 1,250 m downstream (A2–A4) reacted with a rise of 0.1 m.

Water temperature measurements suggest that the water in piezometer A37 throughout the whole experiment, as well as the water in piezometer A26 during the *maximum* pumping regime, was governed by infiltrating SW (Figure 3). The temperatures at all other GW measurement locations correspond to the average annual air temperature of the catchment (8°C), which is typical for shallow GW.

3.2. Results of the SW-GW Simulations

The dominant steady state flow directions of the $n_{aq} = 0.1$, $K_{rb} = 2.4$ m/d scenario simulated for the *maximum* (Figure 4a) and the *minimum* (Figure 4b) pumping regime are illustrated based on stream traces that follow the Darcy velocity field. The distribution of exchange fluxes within the channel and the SW fraction within the aquifer are shown in Figure 5 for all three K_{rb} scenarios (i.e., 0.24 m/d, $K_{rb} = 2.4$ m/d, and $K_{rb} = 24$ m/d; $n_{aq} = 0.1$). Overall, the stream traces in Figure 4 show that the predominant flow direction in the aquifer is horizontal, except where river water infiltrates into the aquifer. While the initial movement of infiltrating SW is vertical, once that water arrives at the depth of the pumps, the subsequent movement is horizontal. The SW-GW exchange fluxes illustrated in Figure 5 reveal alternating sections of gaining and losing conditions. In the upstream part of the model, until the Emme River reaches $Y = 195{,}900$, the exchange fluxes are dominated by two weirs (indicated by the strong black lines crossing the river): directly upstream of the weirs losing conditions dominate, while directly downstream of the weirs gaining conditions prevail. This is in full agreement with the observations of Käser and Hunkeler (2015). The simulated increase in SW discharge matches the observed gaining conditions between Emme St. 1 and Emme St. 2 (see Figure 2). The exchange fluxes vary much stronger as a function of K_{rb} than in response to a change of the pumping regime; and while the pattern of exchange fluxes changes only slightly, the magnitude of exchange is substantially different as a function of K_{rb}. The flow paths in the subsurface, on the other hand, are controlled by the pumping regime: while during *maximum* pumping the subsurface water flow direction tends to strongly bend toward the pumping wells (Figure 4a), under *minimum* pumping the flow direction is more parallel to the valley (Figure 4b).

The different simulations indicate a strong dependency of the pumped water mix on K_{rb}, and to a lesser extent on n_{aq} and on the pumping rates. For the three different simulated states *maximum*, *trans*, and *minimum*, the contribution of recently infiltrated SW to the pumped water mix in wells 1, 5, and 7 are shown in

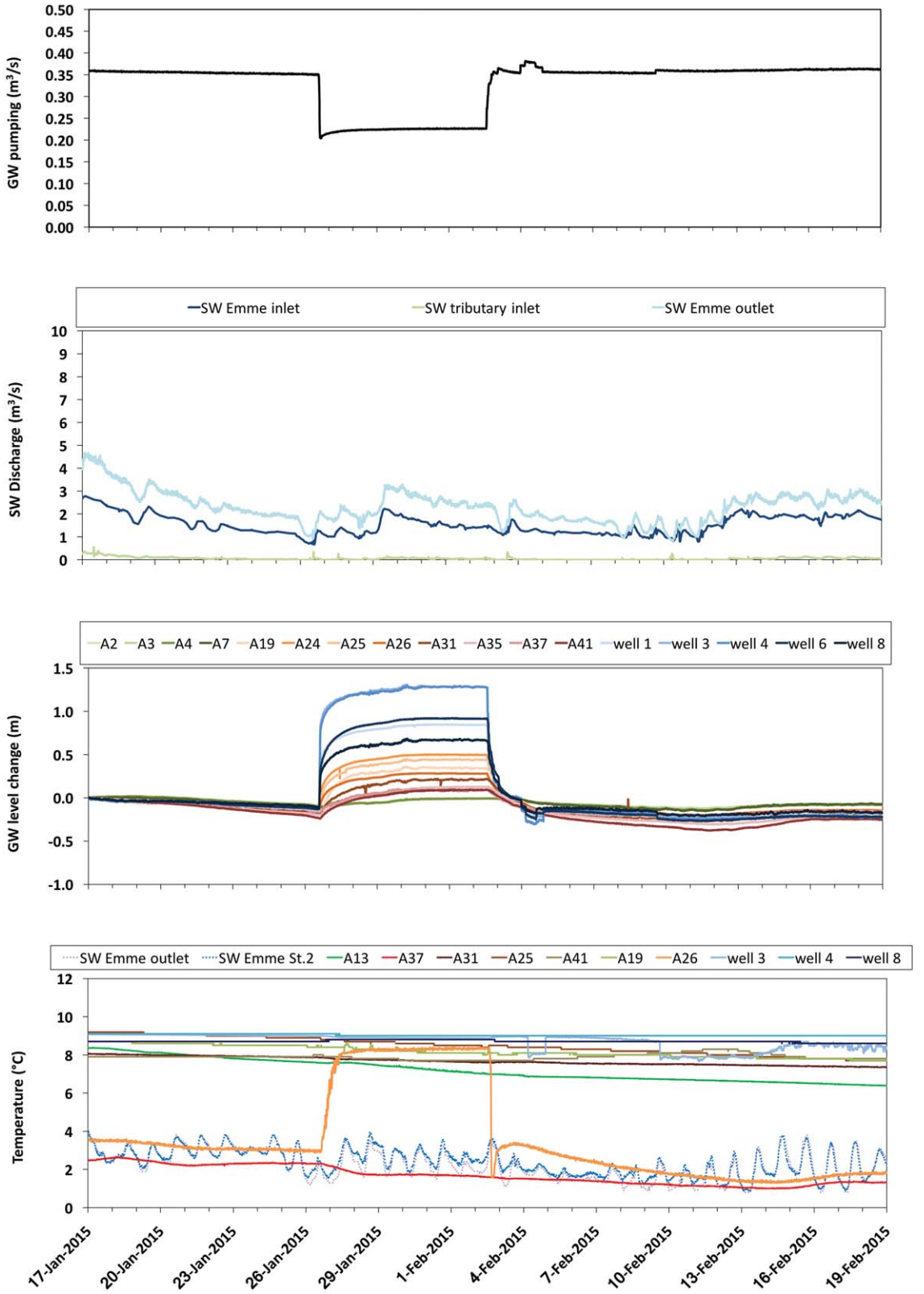

Figure 3. Measured classical observations during the period of the pumping experiment: the pumping rate, the SW discharge at three different measurement stations, the hydraulic heads throughout the study area, and water temperature. GW level changes are given relative to the levels of 17 January 2015 00:00.

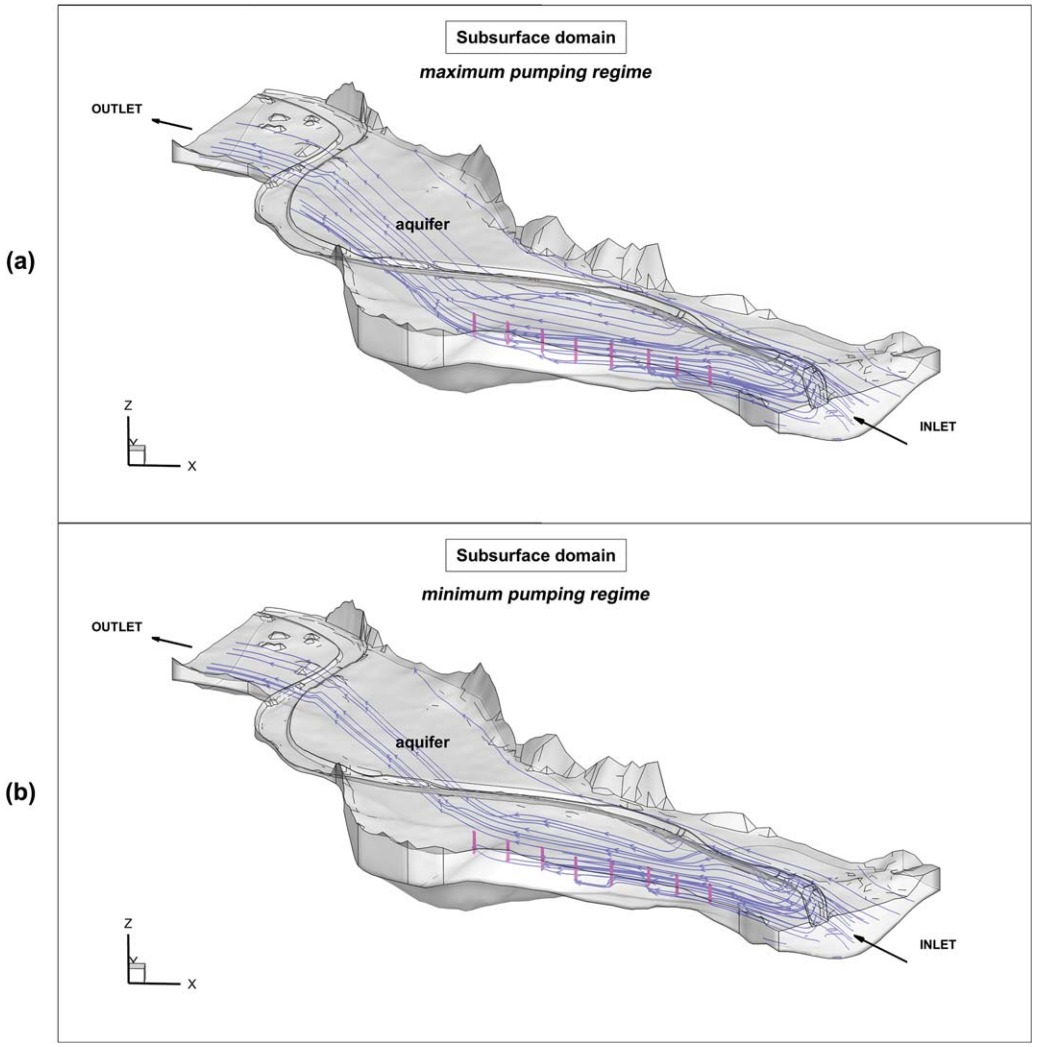

Figure 4. Steady state flow fields of the $n_{aq} = 0.1$, $K_{rb} = 2.4$ m/d scenario. Illustrated are the GW flow directions based on stream traces (blue lines) that follow the Darcy velocity field: (a) *maximum* pumping regime and (b) *minimum* pumping regime.

Table 1. Recall that the recently infiltrated SW water component in the pumped water mix represents water that entered the model domain from the upstream (specified flux) SW boundary condition, and which subsequently infiltrated from the river through the riverbed into the aquifer within the model domain. The remaining part of the pumped water mix is made up by older GW, that is, water that entered the model domain from the upstream (specified head) GW boundary condition.

Although the differences in root-mean-square-error of hydraulic heads ($RMSE_{GW}$) between the different scenarios are very small, Table 1 and Figure 5 clearly show that the mix of pumped water is different between all three K_{rb} scenarios: In terms of the $RMSE_{GW}$, the two scenarios with higher riverbed permeability ($K_{rb} = 2.4$ m/d and $K_{rb} = 24$ m/d) perform similarly and slightly better than the low permeability scenarios ($K_{rb} = 0.24$ m/d). However, the pumped water in the $K_{rb} = 0.24$ m/d scenario is completely dominated by GW, in the $K_{rb} = 24$ m/d scenario by SW, and in the $K_{rb} = 2.4$ m/d scenario the pumped water is made up of approximately equal amounts of GW and SW. The results show that the more is pumped and the further downstream the well is located, the less water from the GW inflow BC is available, and the more freshly infiltrated SW from the SW inflow BC is drawn toward the pumps to satisfy the demand. Simulations of the *maximum* regime showed a substantially larger SW component in the pumped water mix compared to simulations of the *minimum* regime. The largest change in the pumped water mix in response to a reduction of pumping could be observed between the *maximum* to the *minimum* state of $K_{rb} = 2.4$ m/d scenario,

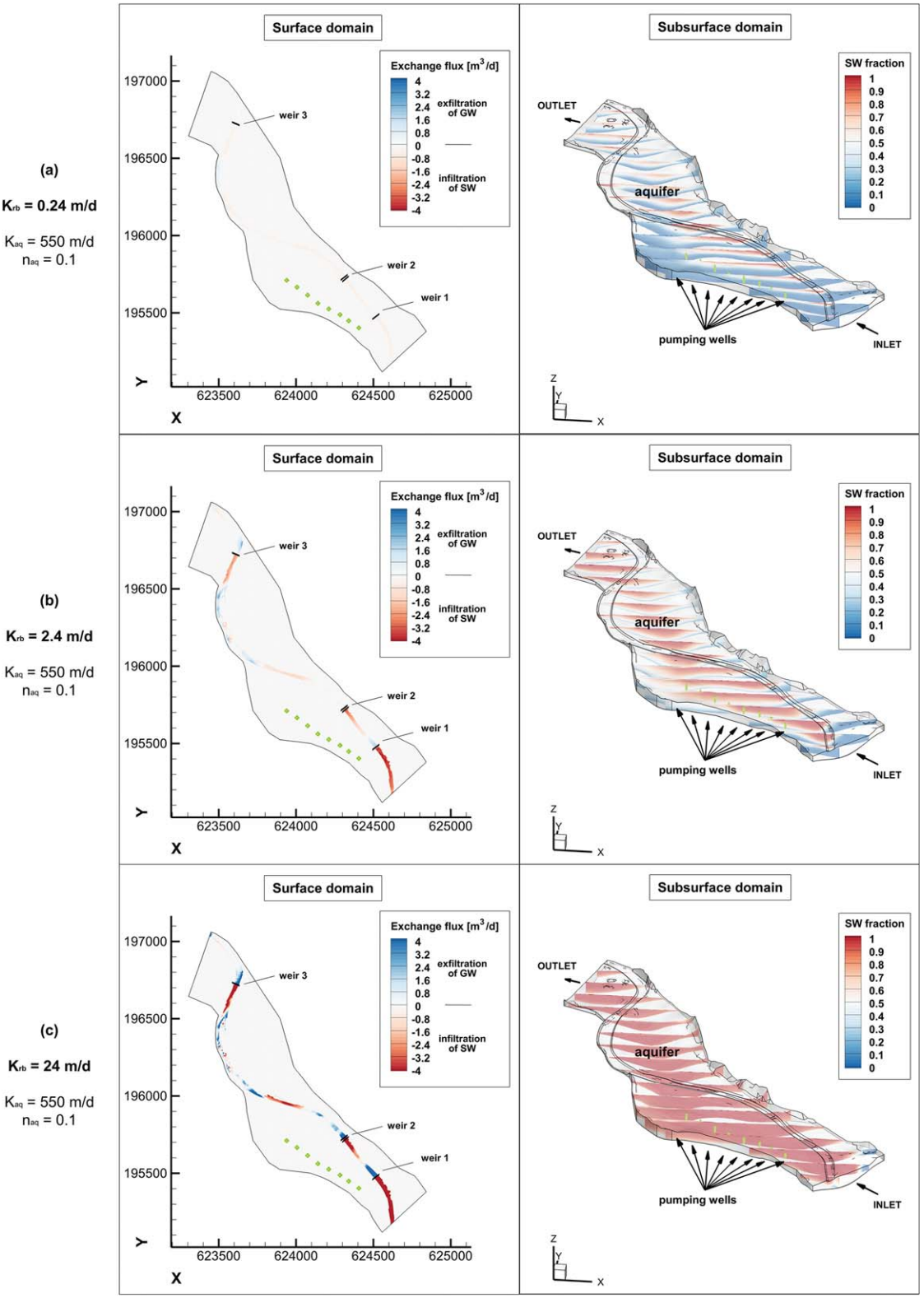

Figure 5. SW-GW exchange fluxes in the river (surface domain) and SW fraction in the aquifer (subsurface domain). (a) Low permeability scenario (K_{rb} = 0.24 m/d), (b) intermediate permeability scenario (K_{rb} = 2.4 m/d), and (c) high permeability scenario (K_{rb} = 24 m/d). Steady state solution for the *maximum* pumping condition is shown. Exchange fluxes represent linearly interpolated nodal values (flux per nodal polygon in m^3/d). Positive exchange fluxes represent gaining conditions (blue), negative exchange fluxes represent losing conditions (red). Weirs are indicated by the solid black lines. Wells are indicated in green; the well numbering was provided in Figure 2. The predominant flow direction for both SW and GW is North-West. North is indicated by the positive *y* direction.

Table 1
Overview of the Contribution of Recently Infiltrated SW to the Pumped Water Mix, the RMSE Between Simulated and Observed Hydraulic Heads ($RMSE_{GW}$ for Wells A3, A4, A7, A19, A24, A25, A26, A31, A35, and A37), and the Travel Times of the Pumped, Recently Infiltrated SW Component for the Three Sampled Wells 1, 5, and 7

		$RMSE_{GW}$				Mean travel time of the SW component in the pumped water			SW fraction in the pumped water mix		
K_{rb} scenario	Regime	$n_{aq} = 0.1$	$n_{aq} = 0.2$	$n_{aq} = 0.43$	Well	$n_{aq} = 0.1$	$n_{aq} = 0.2$	$n_{aq} = 0.43$	$n_{aq} = 0.1$	$n_{aq} = 0.2$	$n_{aq} = 0.43$
$K_{rb} = 0.24$ m/d	*Max*		0.5		Well 1	15	30	40		0.02	
					Well 5	50	65	80		0.10	
					Well 7	60	75	100		0.21	
	Trans	0.44	0.46	0.49	Well 1				0.01	0.01	0.02
					Well 5				0.07	0.08	0.09
					Well 7				0.19	0.20	0.22
	Min		0.42		Well 1	30	35	45		0.01	
					Well 5	65	75	95		0.06	
					Well 7	80	95	140		0.14	
$K_{rb} = 2.4$ m/d	*Max*		0.30		Well 1	15	20	35		0.38	
					Well 5	40	50	75		0.70	
					Well 7	55	70	95		0.77	
	Trans	0.33	0.33	0.33	Well 1				0.29	0.31	0.34
					Well 5				0.58	0.64	0.67
					Well 7				0.80	0.79	0.78
	Min		0.32		Well 1	20	30	40		0.26	
					Well 5	50	65	85		0.51	
					Well 7	65	85	110		0.73	
$K_{rb} = 24$ m/d	*Max*		0.26		Well 1	15	20	30		0.97	
					Well 5	40	50	70		0.98	
					Well 7	50	70	90		1.00	
	Trans	0.31	0.31	0.31	Well 1				0.92	0.94	0.96
					Well 5				0.95	0.96	0.97
					Well 7				1.00	1.00	1.00
	Min		0.31		Well 1	15	25	35		0.89	
					Well 5	45	60	80		0.90	
					Well 7	60	80	100		0.96	

Note. Results are given for the two steady state models (*max* and *min*) and the transient model outputs from the end of the *minimum pumping* regime (*trans*), and separated into the three K_{rb} and three n_{aq} scenarios. The mean travel time of the SW component in the pumped water represents the time at which the SW component has reached 50% of its final contribution to pumped water. Travel time analysis was only carried out for steady state models. Since the $RMSE_{GW}$ is independent of the value of n_{aq} in steady state, it is therefore represented by one single value. The same is also the case for the SW fraction to the pumped water mix.

where shifts of 12%, 19%, and 4% were simulated in wells 1, 5, and 7, respectively (Table 1). For the *transient* scenarios, the smallest porosity models ($n_{aq} = 0.1$) approach the observed differences in the pumped water mix after 1 week of reduced pumping the most. The two higher porosity scenarios result in significantly smaller changes after 7 days of reduced pumping compared to the *min* state simulated with the steady state models. In general, smaller n_{aq} result in a faster reaction of the % of SW in the pumped water to a change of the pumping regime.

In terms of the mean travel time of the SW component, the different simulated scenarios show that if more water is pumped the hydraulic gradients are higher and the mean travel times are smaller (*max* versus *min*). Overall, the simulations also indicate that there is a significant spread of travel times between the different pumping, K_{rb} and n_{aq} scenarios, despite the assumption of homogeneous conditions in the aquifer and the comparably limited extent of the model domain. The mean travel time of the SW component varied between 15 and 45 days in well 1, between 40 and 95 days in well 5, and between 50 and 140 days in well 7 (Table 1). In general, smaller n_{aq} result in smaller travel times.

These modeling results reveal that the water mix, travel times and the dynamic reaction to reduced pumping differ considerably between the different K_{rb} and n_{aq} scenarios. K_{rb} strongly influences the mean travel times and the amount of SW in the pumped water mix, and n_{aq} strongly controls the time it takes for the

pumped mix to react to a changed pumping rate. Most strikingly, this significant difference in model behavior is nearly nonexistent in the $RMSE_{GW}$. Both the values of K_{rb} and of n_{aq} therefore appear to be largely insensitive to a calibration against hydraulic heads. Purely relying on the $RMSE_{GW}$ as the model evaluation criterion would favor the $K_{rb} = 24$ m/d model over the other models.

3.3. Environmental Tracer Results

3.3.1. ^{222}Rn

Activities of ^{222}Rn measured in the background piezometer (A41) exhibited a high average activity concentration of 16 Bq/L_{water}, but varied considerably with a 1σ-standard deviation of 2.3 Bq/L_{water}. Except for one sample, all GW samples were within the uncertainty limits of the background activity. This means that, except for one sample, all sampled GW had a ^{222}Rn residence time of more than 12 days. The one GW sample that differed from this general observation was taken in well 1 one day after the beginning of the *minimum* pumping regime (8.0 ± 1.4 Bq/L_{water}). This sample appears to represent a pocket of younger water. With an average activity of 3.7 ± 1.3 Bq/L_{water} the SW samples taken at Emme St. 2 show a significant influence of GW, indicating gaining conditions. A slightly elevated ^{222}Rn activity (1.2 ± 1.1 Bq/L_{water}) could also be observed in the drain of the pumping field (see Figure 2), which drains parts of the uppermost GW away from the wellfield. The SW samples further upstream correspond to the atmospheric zero activity of ^{222}Rn, which either indicates losing conditions or no SW-GW exchange. In summary, ^{222}Rn indicates GW residence times, or an apparent groundwater age, of at least 12 days at the sampled locations. At the SW measurement stations, ^{222}Rn indicates losing conditions upstream and gaining conditions downstream of the wellfield.

3.3.2. Analysis of Noble Gases and ^{3}H/^{3}He

The results of the ^{3}H and noble gas measurements are presented in Table 2. The measured quantities were used to derive noble gas recharge temperatures, the different helium components, as well as the ^{3}H/^{3}He age according to the methods described in section 2.1. The derived quantities are summarized in Table 3. Due to technical problems during sampling or the gas extraction phase, the samples taken in A19 and in A41, 0–10 m, could not be properly analyzed.

NGRT varies between 3.8 and 7.4°C. The apparent ^{3}H/^{3}He age varies between 0 and 7 years. Excess air is below 100% except for the samples taken in A13. Low ^{3}H/^{3}He age during *maximum* abstraction ($\leq$60 days) and during *minimum* abstraction (1.5 years), low NGRT and very high excess air indicate that piezometer A13 is dominated by very recently infiltrated SW. Its proximity to the Emme River leads to a very rapid exchange with the SW. When less is pumped, less SW appears to infiltrate from the river, and A13 seems to mix with older GW, increasing the apparent ^{3}H/^{3}He age from 0 to 1.5 years. A25 with an apparent ^{3}H/^{3}He age of 7.1 years appears to contain the oldest water. However, A25 exhibits a very low NGRT despite the high apparent ^{3}H/^{3}He age, which makes the interpretation difficult.

The background well A41 has a NGRT of 7.4°C, which is close to the average annual air temperature in the catchment (8°C) and indicates that the old GW component is well mixed. Well 1 has a significantly lower NGRT of 5.7°C, indicating an influence of recently infiltrated SW. Wells 5 and 7 more closely correspond to the NGRT of the background well, revealing a stronger influence of older GW. In reaction to a change of the pumping rate, the NGRT remain relatively constant in wells 1 and 5. The change in NGRT is stronger in well 7, with higher recharge temperatures when less is pumped. The results of the ^{3}H/^{3}He analysis furthermore reveal that the sampled pumping wells are generally controlled by older GW during the *maximum*, and younger GW during the *minimum* pumping regime. Moreover, during the *maximum* pumping regime, the apparent ^{3}H/^{3}He age of GW in the pumping wells is even higher than the water of the background piezometer (A41, 22.5–23.5 m), potentially due to the inflow of deeper GW than the sampling depth of the background piezometer.

The measured isotopic ratios of Ne/^{4}He are plotted against ^{3}He/^{4}He in Figure 6, and the reactions to pumping are indicated by arrows. The GW in the background piezometer (A41, 21.5–23.5 m) appears to have accumulated a significant amount of ^{4}He relative to its initial concentration, thus indicating that this water has resided in the subsurface for the largest amount of time of all sampled GW. The apparent ^{3}H/^{3}He age of the background piezometer suggests that the GW at this location consist of a mix of a very old component with a high amount of ^{4}He and a slightly younger component that pushes the ^{3}H/^{3}He age toward a younger average age compared to the water being pumped in the wells during the *maximum* regime. The pumping wells generally show lower Ne/^{4}He ratios than the piezometers. Compared to ^{3}He/^{4}He, Ne/^{4}He appears to be largely insensitive to a reduction in pumping: while the Ne/^{4}He ratios remain stable, the wells react

Table 2
Summary of the Noble Gas and ^3H Measurements

Location	Sampling	Pumping regime	Time into pumping experiment (days)	Measured quantities: Ar (cm^3 STP/g)	$^{36}Ar/^{40}Ar$	Kr (cm^3 STP/g)	Xe (cm^3 STP/g)	Ne (cm^3 STP/g)	$^{20}Ne/^{22}Ne$	He (cm^3 STP/g)	^3He (cm^3 STP/g)	$^3He/^4He$	^4He (cm^3 STP/g)	Ne/^4He	^3H (TU)	Err. ^3H (TU)
A41, 21.5–23.5 m	22.01.2015 12:31	*Max*		4.02E-04	0.00338	9.33E-08	1.32E-08	2.33E-07	9.791	5.81E-08	8.10E-14	1.39E-06	5.81E-08	4.01	8.90	0.27
A13	22.01.2015 14:10	*Max*		4.10E-04	0.00338	9.82E-08	1.43E-08	2.08E-07	9.793	4.68E-08	6.27E-14	1.34E-06	4.68E-08	4.44	8.69	0.27
	02.02.2015 10:55	*Min*	7	4.17E-04	0.00338	9.98E-08	1.49E-08	2.10E-07	9.786	4.72E-08	6.62E-14	1.40E-06	4.72E-08	4.45	8.81	0.18
A25	02.02.2015 12:05	*Min*	7	4.19E-04	0.00338	1.01E-07	1.52E-08	2.14E-07	9.802	4.88E-08	7.71E-14	1.58E-06	4.88E-08	4.38	8.76	0.23
Well 1	23.01.2015 10:45	*Max*		4.05E-04	0.00338	9.66E-08	1.41E-08	2.22E-07	9.801	5.30E-08	7.93E-14	1.49E-06	5.30E-08	4.18	8.28	0.22
	29.01.2015 13:20	*Min*	3	4.02E-04	0.00339	9.44E-08	1.40E-08	2.19E-07	9.778	5.27E-08	7.31E-14	1.39E-06	5.27E-08	4.16	8.68	0.18
	02.02.2015 15:15	*Min*	7	4.10E-04	0.00338	9.70E-08	1.41E-08	2.21E-07	9.798	5.27E-08	7.08E-14	1.34E-06	5.27E-08	4.19	8.51	0.18
Well 5	23.01.2015 12:30	*Max*		3.96E-04	0.00338	9.26E-08	1.39E-08	2.22E-07	9.795	5.42E-08	7.79E-14	1.44E-06	5.42E-08	4.09	8.85	0.18
	29.01.2015 16:14	*Min*	3	4.04E-04	0.00339	9.42E-08	1.38E-08	2.24E-07	9.781	5.48E-08	7.73E-14	1.41E-06	5.48E-08	4.08	8.26	0.19
	02.02.2015 14:00	*Min*	7	4.00E-04	0.00338	9.32E-08	1.35E-08	2.23E-07	9.791	5.42E-08	7.39E-14	1.36E-06	5.42E-08	4.12	7.73	0.21
Well 7	23.01.2015 14:15	*Max*		4.02E-04	0.00338	9.50E-08	1.38E-08	2.25E-07	9.795	5.37E-08	8.10E-14	1.51E-06	5.37E-08	4.20	7.85	0.18
	29.01.2015 15:00	*Min*	3	3.92E-04	0.00339	9.16E-08	1.34E-08	2.19E-07	9.789	5.31E-08	7.36E-14	1.39E-06	5.31E-08	4.13	8.21	0.17
	02.02.2015 14:45	*Min*	7	3.95E-04	0.00339	9.23E-08	1.34E-08	2.22E-07	9.787	5.30E-08	7.66E-14	1.45E-06	5.30E-08	4.19	8.35	0.17

Note. Except for ^3H with a measurement error of ~3%, all measurements are associated with a measurement error of less than 1.5%. Measurements were made during the *maximum* pumping regime before the beginning of the *minimum* pumping experiment (*max*), as well as during and immediately before the end of the *minimum* pumping experiment (*min*). The time that has passed between the beginning of the *minimum* pumping experiment and the sampling is indicated.

Table 3
Derived Noble Gas Quantities

Location	Sampling	Pumping regime	Time into pumping experiment (days)	$^3H/^3He$ age (years)	Err. $^3H/^3He$ age (years)	Excess air (%)	Air-water frac.	Err. air-water frac. (%)	NGRT (°C)	Err. NGRT (%)	$^3He^*$ (cm^3 STP/g)	Err. $^3He^*$ (%)	$^3He_{atm}$ (cm^3 STP/g)	$^4He_{atm}$ (cm^3 STP/g)	$^3He_{corr}/^4He$ (cm^3 STP/g)
A41, 21.5–23.5 m	22.01.2015 12:31	*Max*		4.38	1.29	59.57	0.494	30.3	7.4	*4.7*	6.17E-15	26.5	5.84E-14	4.29E-08	1.288E-06
A13	22.01.2015 14:10	*Max*		0.00	1.73	202.66	0.899	3.1	5.2	*10.0*	0.00		5.90E-14	4.34E-08	1.339E-06
	02.02.2015 10:55	*Min*	7	1.51	0.82	160.67	0.883	1.4	4.5	*3.3*	1.94E-15	24.9	5.92E-14	4.36E-08	1.361E-06
A25	02.02.2015 12:05	*Min*	7	7.10	0.77	8.82	0.000		3.8	*3.5*	1.07E-14	6.2	5.95E-14	4.37E-08	1.361E-06
Well 1	23.01.2015 10:45	*Max*		6.26	1.62	15.12	0.000		5.7	*7.8*	8.69E-15	31.9	5.89E-14	4.33E-08	1.331E-06
	29.01.2015 13:20	*Min*	3	3.02	1.06	69.26	0.681	11.7	6.5	*3.6*	4.00E-15	22.8	5.86E-14	4.31E-08	1.311E-06
	02.02.2015 15:15	*Min*	7	1.41	1.23	76.13	0.704	9.4	5.7	*3.9*	1.75E-15	57.5	5.89E-14	4.33E-08	1.311E-06
Well 5	23.01.2015 12:30	*Max*		4.96	1.29	30.95	0.391	161.7	7.0	*5.9*	7.08E-15	24.6	5.85E-14	4.30E-08	1.307E-06
	29.01.2015 16:14	*Min*	3	4.89	0.64	82.90	0.667	4.2	6.8	*1.7*	6.51E-15	5.2	5.85E-14	4.30E-08	1.291E-06
	02.02.2015 14:00	*Min*	7	2.63	0.38	72.59	0.640	1.0	7.2	*0.3*	3.06E-15	2.5	5.84E-14	4.30E-08	1.307E-06
Well 7	23.01.2015 14:15	*Max*		6.51	1.26	17.89	0.000		6.3	*3.9*	8.62E-15	17.6	5.87E-14	4.31E-08	1.348E-06
	29.01.2015 15:00	*Min*	3	2.91	0.82	46.20	0.556	13.8	7.5	*1.5*	3.64E-15	13.1	5.83E-14	4.29E-08	1.318E-06
	02.02.2015 14:45	*Min*	7	4.43	0.45	47.19	0.539	4.7	7.4	*0.5*	5.88E-15	2.5	5.84E-14	4.29E-08	1.336E-06

Note. NGRT represents the noble gas recharge temperature. The error of the $^3H/^3He$ water age was calculated according to Visser et al. (2014).

AGU Water Resources Research

10.1002/2017WR020754

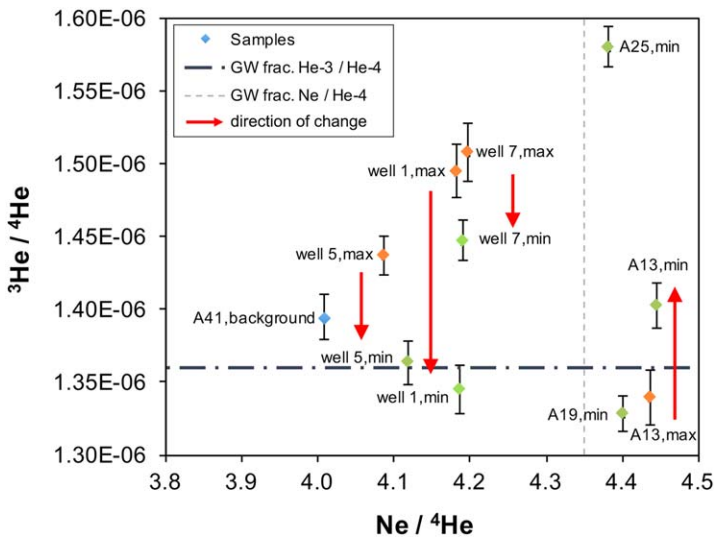

Figure 6. Measured $^3He/^4He$ versus the measured $Ne/^4He$ ratios. For simplification, only the *maximum* and the measurements immediately before the end of the *minimum* regime (i.e., 7 days after the beginning of the *min* pumping experiment) are indicated. The background sample is marked in blue, the *maximum* samples are marked in orange, and the *minimum* samples are marked in green. Reactions to a change in the pumping regime are indicated by red arrows. Error bars represent 1σ-standard deviations. The reader is referred to Tables 2 and 3 for the complete list of measurements.

strongly to the pumping regime in terms of their $^3He/^4He$ ratio, changing from higher ratios during *maximum* to lower ratios during *minimum*. The changes in $^3He/^4He$ to pumping can therefore mainly be attributed to a change in the tritiogenic ^3He ($^3He^*$) content.

While for the *maximum* regime, the wells seem to have a ratio of $^3He/^4He$ that is significantly higher than that of air-equilibrated water, therefore consisting of water that has resided in the subsurface for a longer amount of time, in the *minimum* regime the ratios become smaller and approach the ratio of AEW. The source of the pumped water thus appears to be shifting toward more freshly infiltrated SW during *minimum* compared to during the *maximum* pumping regime. This agrees with the $^3H/^3He$ residence time estimates. The GW in A25 appears to be most enriched in ^3He relative to ^4He, but has not accumulated significant amounts of ^4He. While this agrees with the $^3H/^3He$ age, the reason for this is unclear. A13 during *maximum* pumping shows the lowest enrichment of ^3He relative to ^4He and AEW, as well as the lowest ratio of $Ne/^4He$. This again reveals a strong influence of recently infiltrated SW at this location. In accordance with the $^3H/^3He$ and NGRT results, during *maximum* pumping A13 is more controlled by recently infiltrated SW compared to during *minimum* pumping.

3.3.3. ^{37}Ar

The measured activity concentrations of ^{37}Ar are summarized in Table 4 and illustrated in Figure 7 as a function of their sampling depth. The samples from the depth profile of the background piezometer A41 show an exponentially decreasing activity with increasing depth, which agrees with the theory of ^{37}Ar production. This allows the following assumptions to be formulated:

1. Water in the background piezometer has reached the secular equilibrium of ^{37}Ar (which is supported by the noble gas analyses).
2. Flow at A41 is mainly horizontal (which is confirmed by the numerical model results provided in section 3.2).

Based on these two assumptions, the equilibrium profile and the corresponding attenuation length could be identified (i.e., 15.9 m) and residence times isolines of 1 week, 1 month, and 3 months could be

Table 4
Summary of the ^{37}Ar Measurement Results

Location	Sampling	Pumping regime	$^{37}Ar_{eq}$ (mBq/L_{water})	Err. $^{37}Ar_{eq}$ (mBq/L_{water})	^{37}Ar (mBq/L_{water})	Err. ^{37}Ar (%)	$^{37}Ar/^{37}Ar_{eq}$	Err. $^{37}Ar/^{37}Ar_{eq}$
A41, 0–10 m	17.03.15	*Max*	3.19E-03	5.8E-4	2.95E-03	11	0.92	0.19
A41, 11.5–13.5 m	17.03.15	*Max*	2.25E-03	3.5E-4	2.23E-03	11	0.99	0.19
A41, 16–18 m	17.03.15	*Max*	1.69E-03	2.7E-4	1.45E-03	11	0.85	0.16
A41, 21.5–23.5 m	17.03.15	*Max*	1.20E-03	2.2E-4	1.28E-03	11	1.07	0.22
Emme Aeschau	09.04.14	*Max*	n/a	n/a	1.36E-04	0	n/a	n/a
A13	09.04.14	*Max*	3.57E-03	6.9E-4	2.36E-03	12	0.66	0.15
A25	09.12.14	*Max*	3.23E-03	5.9E-4	8.70E-04	28	0.27	0.09
A26	09.12.14	*Max*	2.26E-03	4.1E-4	1.90E-03	11	0.75	0.15
A41, 21.5–23.5 m	13.10.15	*Max*	1.20E-03	2.2E-4	1.49E-03	11	1.24	0.27
Well 1	23.01.15 10:45	*Max*	2.26E-03	3.6E-4	1.11E-03	12	0.49	0.10
	02.02.15 15:15	*Min*	2.26E-03	3.6E-4	1.36E-03	11	0.60	0.12
Well 5	23.01.15 12:30	*Max*	1.83E-03	2.8E-4	1.04E-03	12	0.57	0.11
	02.02.15 14:00	*Min*						
Well 7	23.01.15 14:15	*Max*	1.84E-03	2.9E-4	1.89E-03	11	1.03	0.19
	02.02.15 14:45	*Min*	1.84E-03	2.9E-4	1.98E-03	12	1.08	0.21

Note. The corresponding secular equilibrium activity concentrations at the depth of each well are also given. Errors are 1σ-standard deviations, and for $^{37}Ar_{eq}$ correspond to the 1σ-confidence interval.

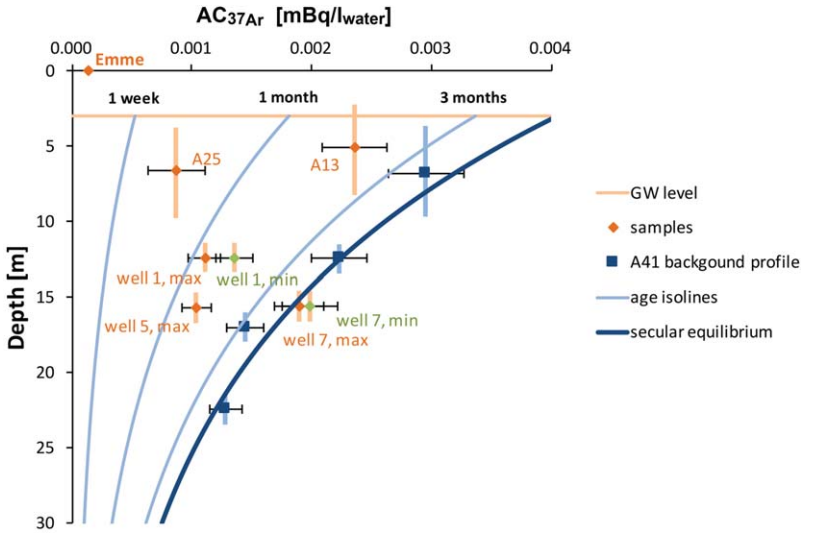

Figure 7. ^{37}Ar activity concentrations as a function of depth. ^{37}Ar age isolines of 1 week, 1 month, and 3 months were derived from the ^{37}Ar background profile in well A41. The green markers represent samples taken immediately before the end of the *minimum* pumping regime and orange markers represent samples taken during the *maximum* pumping regime. The vertical bars indicate the screened depths at each location. Horizontal bars indicate measurement errors.

generated for Figure 7. The small portion of vertical flow of freshly infiltrating SW until it arrives at the depth at which horizontal flow becomes predominant can be considered negligible for the ingrowth of ^{37}Ar. The two pumping wells 1 and 7, which were sampled before and immediately at the end of the *minimum* pumping experiment, show only a very small, and according to the uncertainty limits not significant, increase in ^{37}Ar activity concentration in reaction to the pumping. The ^{37}Ar activity concentration of the Emme River SW in the downstream direction of A13 is considerably smaller compared to the GW samples, but not zero. This agrees with the findings of the ^{222}Rn measurements and confirms that at this location GW is exfiltrating into the river. The fact that the activity concentration for the samples in wells 1 and 5, as well as in piezometers A13 and A25, is between the secular equilibrium and zero activity leads to the conclusion that there is a substantial component of freshly infiltrated SW with a residence time between multiple days to 3.5 months (i.e., 110 days) in the sampled GW mix.

If translated into residence times, the ^{37}Ar activities suggest that the sampled water has average apparent ^{37}Ar residence times of approximately 1.5 month in wells 1 and 5, and more than 3.5 months in well 7. If the pumped water were entirely composed of freshly infiltrated SW, the average age of the freshly infiltrated SW and the average age of the water in the respective wells would be identical. However, based on the results from the other tracers, it seems more likely that the pumped water represents a mix between freshly infiltrated SW and older GW. In this case, the residence time of the freshly infiltrated SW must be smaller than the apparent average ^{37}Ar residence time of the samples: the range of possible average residence times for the freshly infiltrated SW in the two pumping wells 1 and 5 lies between the apparent ^{222}Rn residence time (12 days) and the apparent ^{37}Ar residence time (1.5 months). In well 7, ^{37}Ar has reached the secular equilibrium and the minimum residence time in well 7 is therefore equal to or larger than 3 times the half-life of ^{37}Ar (i.e., $\geq$110 days).

3.3.4. Tracer-Based Analysis of the Mixing Ratios

Both NGRT and $^{3}He_{corr}/^{4}He$ can be assumed stable during the travel times encountered within the drinking water wellfield, i.e., there is no production or decay during a time scale from a few days to 3–4 months. They are therefore suited for end-member mixing analysis between different water components within the studied SW-GW system:

1. *NGRT*. The two end-members for NGRT are given by (1) freshly infiltrated SW with a NGRT corresponding to the SW water temperature during the residence time range of the SW component in the corresponding well and (2) the GW in the background piezometer A41 (7.4°C, see Table 3). The end-member for SW were chosen according to the residence time range found in the ^{37}Ar analysis, which suggests that the

Table 5
Estimations of the Contribution of Recently Infiltrated SW in the Water Mix Based on the Analysis of Two Different Environmental Tracer-Based Indicators (NGRT and $^3He_{corr}/^4He$)

Sampling location	Pumping regime	SW component in the sampled water mix	
		NGRT based (%)	$^3He_{corr}/^4He$ based (%)
A13	*Max*	61	71
	Min	78	100
A25	*Max*		
	Min	75	100
Well 1	*Max*	46	60
	Min	45	32
Well 5	*Max*	10	26
	Min	8	26
Well 7	*Max*		83
	Min		67

Note. The end-members for this analysis were chosen according to end-members relevant in the drinking water wellfield and in the SW-GW model.

SW components in well 1 and 5 have a residence time between 12 days and 1.5 months. The average SW temperature during the 2 months prior to the pumping experiment was 3.7°C. For A13 the same recharge temperature as for wells 1 and 5 was used, whereas for A25 the average SW temperature during the pumping experiment (i.e., 2.8°C). The NGRT mix was quantified with equation (8).

2. $^3He_{corr}/^4He$. The two end-member ratios are given by (1) freshly infiltrated SW with a ratio corresponding to AEW (1.36×10^{-6}) and (2) the GW in the background piezometer A41 with a $^3He_{corr}/^4He$ ratio of 1.288×10^{-6} (see Table 3). The $^3He_{corr}/^4He$ mix between the two end-members was calculated with equation (9).

The tracer-based mixing fractions between recently infiltrated SW and older GW are summarized in Table 5. The two tracer-based mixes are comparable: both tracers show that the water mix pumped by the three wells consists of approximately equal parts of freshly infiltrated SW and GW, rather than consisting purely of older GW or purely of freshly infiltrated SW. The water in well 1 appears to be made up of more SW than the water in well 5, whereas well 7 is again more SW influenced than well 5. $^3He_{corr}/^4He$ suggests a strong reaction to a reduction of the pumping rate in both well 1 and well 7: −28% and −16% SW, respectively. NGRT only suggests a strong reaction in A13 (–19%), but not in well 1 or well 5. Overall, $^3He_{corr}/^4He$ suggests slightly more SW influence compared to NGRT.

3.4. Improving the Model Using Measured and Simulated Residence Times and Mixing Ratios

A comparison of the simulated mean travel times of the SW component in the pumped water (Table 1) to the tracer-based residence times (Table 6) shows that all models are in accordance with the ^{222}Rn-based measurements: the mean travel times exceed the 12 days required for ^{222}Rn to reach equilibrium. Moreover, as the model does not simulate the complete catchment but only the vicinity of the wellfield, the simulated travel times cannot be compared directly to the $^3H/^3He$ residence times. Consequently, based on ^{222}Rn and $^3H/^3He$, a clear identification of the best model parametrization would be impossible. Residence times estimates based on the novel ^{37}Ar tracer method, on the other hand, allow overcoming this problem by covering the relevant time scale of the investigated SW-GW system: In general, the $n_{aq} = 0.1$ models are best for the reproduction of the mean travel times in well 5, whereas the $n_{aq} = 0.2$ models reproduce the travel times for well 1 better, and the $n_{aq} = 0.43$ models the travel times for well 7. While the best overall reproduction of the tracer-based mean travel times estimates can tentatively be attributed to the $K_{rb} = 2.4$ m/d scenario, even with ^{37}Ar-based residence times a clear distinction of the most appropriate model parametrization is still difficult.

The most appropriate model parametrization becomes evident only when tracer-based and simulated mixing ratios between freshly infiltrated SW and older GW are compared: a comparison of the measured SW fraction (Table 5) to the simulated SW fraction (Table 1) in A13, A25 and wells 1, 5, and 7 clearly reveals that out of the three tested K_{rb} scenarios, only the $K_{rb} = 2.4$ m/d model is appropriate for the simulation of the drinking water wellfield. This is illustrated in Figure 8, where both the $^3He_{corr}/^4He$-based and the simulated SW fraction are plotted. Both the $K_{rb} = 0.24$ m/d and $K_{rb} = 24$ m/d model do not allow the reproduction of the tracer-based mixing ratios between freshly infiltrated SW and GW, and result in a severe underestimation (<10% SW) or a severe overestimation (>90% SW) in the pumping wells, respectively. The comparison of the mixing ratios furthermore allows the identification of the most appropriate n_{aq} value: in terms of the changes in the pumped water mix in reaction to 7 days of reduced pumping, the $K_{rb} = 2.4$ m/d, $n_{aq} = 0.1$, *trans* model best approaches the magnitude of changes observed in the tracer measurements.

Based on these findings, the most appropriate model parametrization can only be evaluated if the mixing ratios are considered. This allows

Table 6
Comparison of Tracer-Based Apparent Residence Times at Key Sampling Locations According to the Three Tracers Employed

Location	Pumping regime	Apparent residence times		
		^{222}Rn (days)	^{37}Ar (days)	$^3H/^3He$
A41, 21.5–23.5 m	*Max*	≥12	≥110	4.4 years
A13	*Max*	≥12	54	≤60 days
	Min	≥12		1.5 years
A25	*Max*	≥12	16	
	Min	≥12		7.1 years
Well 1	*Max*	≥12	34	6.3 years
	Min	≥12	46	1.4. years
Well 5	*Max*	≥12	42	5.0 years
	Min	≥12		2.6 years
Well 7	*Max*	≥12	≥110	6.5 years
	Min	≥12	≥110	4.4 years

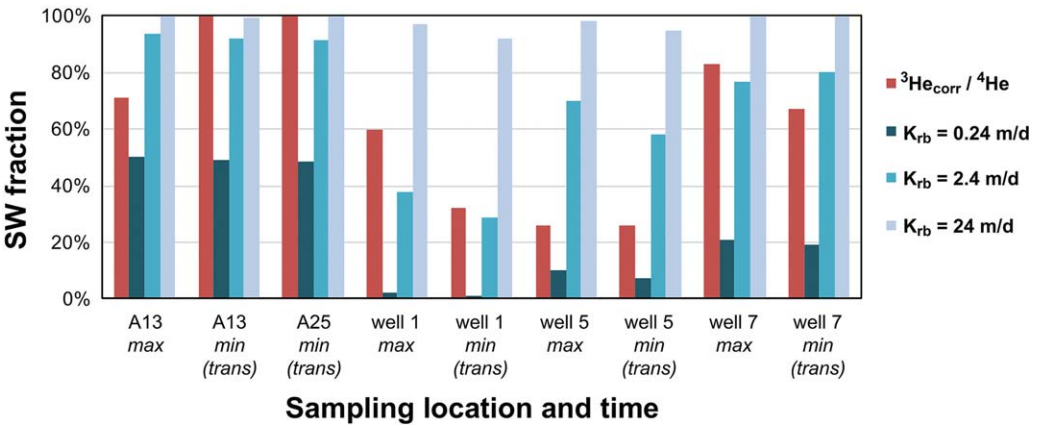

Figure 8. Comparison between the $^3He_{corr}/^4He$-based SW fraction and the simulated SW fraction. The *max* measurements are compared to the steady state *max* simulations, and the *min* measurements are compared to the *trans* simulations.

identifying the $K_{rb} = 2.4$ m/d, $n_{aq} = 0.1$ model as the most appropriate parametrization. The tracer-based mixes furthermore hint at a potential structural problem of the model: while the influence of SW in the pumped water increases with increasing distance of the pumping well to the river (i.e., the SW component is highest in well 7), the measured mix suggests that this only holds true for wells 1 and 7. In well 5, on the other hand, much less SW is pumped compared to well 1 (shown by both NGRT and $^3He_{corr}/^4He$) and compared to well 7 (shown by $^3He_{corr}/^4He$). This structural problem is most likely due to the simplifying assumption of a homogeneous K_{aq}.

4. Discussion

We integrated a multitracer study of an important alluvial drinking water station with physically-based flow modeling. The multitracer investigation consisted of measurements of ^{222}Rn, $^3H/^3He$, atmospheric noble gases, and ^{37}Ar measurements. ^{37}Ar has never been used as a tracer for residence times in SW-GW systems before. While the classic tracers ^{222}Rn and $^3H/^3He$ could have been explained by the presence of only one type of water, the fact that the ^{37}Ar and $^3H/^3He$ dating methods resulted in different residence times revealed that the sampled water consisted of a mix of two different water types: (a) one type constitutes freshly infiltrated SW that has resided in the subsurface on time scales to which only ^{37}Ar is sensitive (i.e., between 2 weeks and 3.5 months). (b) Another type constitutes older GW that has resided in the subsurface on larger time scales to which ^{37}Ar is not sensitive anymore, but that is detectable by $^3H/^3He$ (i.e., 3.5 months to multiple years). Thus, through the combined application of the ^{222}Rn, ^{37}Ar and $^3H/^3He$ dating methods, for the first time residence times of water types (a) and (b) could be constrained. The combined application of these three tracers furthermore allowed identifying suitable tracers for the analysis of end-member mixing: NGRT and $^3He_{corr}/^4He$.

With the addition of ^{37}Ar, an important observational gap in the analysis of residence times could be closed—a residence time scale which is of particular importance in alluvial SW-GW systems. Including ^{37}Ar allowed constraining the travel time of freshly infiltrated SW between the Emme River and the GW wells, and helped identifying the end-members for the mixing analysis; as outlined above, this would not have been possible with other tracers for residence times such as ^{222}Rn or $^3H/^3He$, which are insensitive to the relevant residence times. One complication for the application of ^{37}Ar as a dating tool in SW-GW systems is the depth-dependency of the production of ^{37}Ar. As opposed to dating using ^{222}Rn, a correct interpretation of ^{37}Ar measurements therefore requires the predominant flow directions in the subsurface to be identified. For this purpose, we used a physically-based numerical flow model, with the ability to simulate SW-GW interactions in a fully-integrated way. The flow simulations clearly showed that horizontal subsurface fluxes dominate, except for the moment at which SW infiltrated into the subsurface. The ingrowth of ^{37}Ar during this vertical movement of the water parcel is, however, negligible for the overall ingrowth of ^{37}Ar. The combined application of ^{37}Ar measurements together with fully-integrated flow modeling allowed us to interpret the ^{37}Ar measurements under the assumption of horizontal subsurface flow, and substantially

facilitated the analysis. Even though sampling for ^{37}Ar requires a relatively large volume of water to be degassed directly in the field and the depth dependency of the production of ^{37}Ar to be determined locally, the insights gained from ^{37}Ar are extremely useful.

Neither the classic measurements of GW levels and SW discharge, nor the residence time analysis based on the three different dating methods, allowed a clear identification of an appropriate flow model parametrization. However, for a comprehensive simulation and prediction of flow paths and mixing ratios, identifying an appropriate model parametrization is imperative. To overcome this gap, we used the residence time tracers to identify ideal tracers for an end-member mixing analysis. We then compared these tracer-based mixing ratios to simulated mixing ratios of multiple different model parametrizations that were all well-calibrated against hydraulic heads by means of $RMSE_{GW}$, but that strongly differed in the hydraulic conductivity of the riverbed (K_{rb}) and the porosity of the aquifer (n_{aq}). While all models performed similarly well in reproducing the hydraulic heads, the models strongly differed in the simulation of the pumped water mix (see Table 1). The tracer-based mixing ratios allowed identifying that out of the three different K_{rb} scenarios, only the intermediate permeability scenario allowed reproducing the tracer-based mixing ratios (see Figure 8). Moreover, out of the three different n_{aq} scenarios, only the lower porosity scenarios resulted in similarly rapid changes of mixing ratios in response to a change in the pumping regime as observed with the tracer-based measurements. Identifying the shortcomings of the inappropriately parametrized models would, in this case, not have been possible by analyzing hydraulic heads or residence times alone. The analyses of the environmental tracers also allowed detecting potential structural issues in the model: instead of simulating a stronger influence of SW in the wells closer to the river, the models suggested the opposite, i.e., that the wells further away from the river are more strongly influenced by SW. This difference between the tracer measurements and the simulations might suggest that the assumption of homogeneity for K_{aq} is not justified, and that mild heterogeneity exists.

Our study highlights that (1) tracer-based estimates of mixing ratios and residence times provide valuable information concerning alluvial SW-GW systems and help to identify appropriate flow model parametrizations for these systems, (2) that it is necessary to choose tracers with a sensitivity to the expected time scales of the investigated system (which is in accordance with the interpretation of Larocque et al. (2009), among others), (3) that ^{37}Ar can close the gap in residence times characterizations required for alluvial SW-GW systems, and (4) that multiple tracers need to be applied in order to estimate both mixing ratios and residence times simultaneously.

5. Conclusions

We successfully closed an existing observational gap in the characterization of residence times of SW-GW systems by combining the existing tracer methods of ^{222}Rn, $^{3}H/^{3}He$ and noble gases with ^{37}Ar. By using the novel ^{37}Ar-method, we could detect recently infiltrated SW in the wellfield of an important drinking water station situated in an alluvial SW-GW system. This SW component would have been missed by the existing tracer methods. As a result of this, we could identify suitable tracers for end-member mixing analysis in such SW-GW systems (i.e., NGRT and He isotope ratios). The end-member mixing analysis served as the basis for the quantification of the fraction of recently infiltrated SW in the subsurface.

Moreover, we coupled the tracer-based analyses with complex physically-based SW-GW modeling. We used the fully-coupled SW-GW flow simulator HydroGeoSphere and coupled it to the Hydraulic Mixing-Cell flow tracker, which allowed tracking water from all sources throughout the entire modeling domain without much additional computational costs. These simulations not only provided the basis for the interpretation of the tracer measurements, the unconventional tracer observations also allowed to identify a more appropriate flow model parametrization by comparing the measured, tracer-based end-member mixing ratios to simulated mixing ratios. We could demonstrate that identifying appropriate values for the hydraulic conductivity of the riverbed and porosity of the aquifer—key parameters for residence times and mixing ratios—would not have been possible based on classic observations of hydraulic heads alone. While the combination of end-member mixing ratios and hydraulic head data suggests that a homogeneous parametrization of the flow model with low, transport effective porosity values could be appropriate, a heterogeneous system with preferential flow paths and higher total porosity could exist in reality. To conclude

whether such a system does exist yet more complex modeling approaches including heterogeneous structures should be evaluated against the combination of isotopic and hydraulic observations.

So far, the combination of all these tracers in a multitracer study and the combination of complex flow models with such multitracer studies are an exception, but indicate the direction for future applications, as also pointed out by Turnadge and Smerdon (2014). Our study provides a closure of the long existing residence times gap in SW-GW systems, and is a demonstration of the largely unexplored potential of end-member mixing ratios in informing SW-GW model construction and calibration.

Acknowledgments
The authors thank L. Tyroller, E. Ghadiri, Y. Tomonaga, A. Popp, J. Oser, S. Figura, I. Beck, and W. Wild from EAWAG for their support in the noble gas laboratory and during sampling, and A. Badin, C. Carlier, P. Wanner, A. Schomburg, R. Costa, and L. Marguet from the CHYN for their assistance during the extensive sampling campaign. The authors are very thankful to B. Gyger, B. Burkhalter, B. Wysmüller, and R. Hirschi from the WVRB for making the pumping experiment possible. We are thankful to the Editor Jean Bahr as well as the Associate Editor and three anonymous reviewers for their insightful comments and feedback. Oliver S. Schilling is grateful for the partial funding received from the Swiss National Science Foundation grant P2NEP2_171985. All data are provided in the manuscript. The basic model input files required to run the transient model of the $K_{rb} = 2.4$ m/d, $n_{aq} = 0.1$ parametrization are provided as supporting information data set S1.

References

Aeschbach-Hertig, W., Peeters, F., Beyerle, U., & Kipfer, R. (1999). Interpretation of dissolved atmospheric noble gases in natural waters. *Water Resources Research*, *35*(9), 2779–2792.

Aeschbach-Hertig, W., & Solomon, D. K. (2013). Noble gas thermometry in groundwater hydrology. In P. Burnard (Ed.), *Advances in isotope geochemistry*. Berlin, Germany: Springer.

Åkesson, M., Suckow, A., Visser, A., Sültenfuß, J., Laier, T., Purtschert, R., & Sparrenbom, C. J. (2015). Constraining age distributions of groundwater from public supply wells in diverse hydrogeological settings in Scania, Sweden. *Journal of Hydrology*, *528*, 217–229.

Ala-Aho, P., Soulsby, C., Wang, H., & Tetzlaff, D. (2017). Integrated surface-subsurface model to investigate the role of groundwater in headwater catchment runoff generation: A minimalist approach to parameterisation. *Journal of Hydrology*, *547*, 664–677.

Althaus, R., Klump, S., Onnis, A., Kipfer, R., Purtschert, R., Stauffer, F., & Kinzelbach, W. (2009). Noble gas tracers for characterisation of flow dynamics and origin of groundwater: A case study in Switzerland. *Journal of Hydrology*, *370*, 64–72.

Anderson, M. P., Woessner, W. W., & Hunt, R. J. (2015). *Applied groundwater modelling* (2nd ed.). Oxford, UK: Academic Press.

AWA (2013). *Amt für Wasser und Abfall des Kantons Bern: Isohypsen des Grundwasserstauers (GW25)*. Bern, Switzerland: AWA. Retrieved from https://www.map.apps.be.ch

Aquanty Inc (2016). *HydroGeoSphere. A Three-dimensional numerical model describing fully integrated subsurface and surface flow and solute transport*. Waterloo, ON: Aquanty Inc.

Banks, E. W., Brunner, P., & Simmons, C. T. (2011). Vegetation controls on variably saturated processes between surface water and groundwater and their impact on the state of connection. *Water Resources Research*, *47*, W11517. https://doi.org/10.1029/2011WR010544

Bauser, G., Hendricks Franssen, H. J., Kaiser, H.-P., Kuhlmann, U., Stauffer, F., & Kinzelbach, W. (2010). Real-time management of an urban groundwater well field threatened by pollution. *Environmental Science & Technology*, *44*, 6802–6807.

Bertrand, G., Celle-Jeantont, H., Huneau, F., Loock, S., & Renac, C. (2010). Identification of different groundwater flowpaths within volcanic aquifers using natural tracers for the evaluation of the influence of lava flows morphology (Argnat basin, Chaîne des Puys, France). *Journal of Hydrology*, *391*, 223–234.

Beyerle, U., Aeschbach-Hertig, W., Hofer, M., Imboden, D. M., Baur, H., & Kipfer, R. (1999). Infiltration of river water to a shallow aquifer investigated with $^3H/^3He$, noble gases and CFCs. *Journal of Hydrology*, *220*, 169–185.

Beyerle, U., Aeschbach-Hertig, W., Imboden, D. M., Baur, H., Graf, T., & Kipfer, R. (2000). A mass spectrometric system for the analysis of noble gases and tritium from water samples. *Environmental Science & Technology*, *34*, 2042–2050.

Biaggi, D., Polack, P., & Backman, N. (2005). *Grundwasserfassungen Aeschau—Gesuch um Konzessionserneuereung—Fachbericht Hydrologie/Hydrogeologie*. Bern, Switzerland: Geotechnisches Institut.

Blau, R. V., & Muchenberger, F. (1997). *Grundlagen für Schutz und Bewirtschaftung der Grundwasser des Kantons Bern: Nutzungs-, Schutz- und Überwachungskonzept für die Grundwasserleiter des obersten Emmentals, zwischen Emmenmatt, Langnau und Eggiwil, Synthesebericht*. Bern, Switzerland: Wasser- und Energiewirtschaft des Kantons Bern.

Boano, F., Harvey, J. W., Marion, A., Packman, A. I., Revelli, R., Ridolfi, L., & Wörman, A. (2014). Hyporheic flow and transport processes: Mechanisms, models, and biogeochemical implications. *Reviews of Geophysics*, *52*, 603–679. https://doi.org/10.1002/2012RG000417

Bourke, S. A., Cook, P. G., Dogramaci, S., & Kipfer, R. (2015). Partitioning sources of recharge in environments with groundwater recirculation using carbon-14 and CFC-12. *Journal of Hydrology*, *525*, 418–428.

Bourke, S. A., Cook, P. G., Shanafield, M., & Dogramaci, S., Clark, J. F. (2014). Characterisation of hyporheic exchange in a losing stream using radon-222. *Journal of Hydrology*, *519*, 94–105.

Bredehoeft, J. (2005). The conceptualization model problem—Surprise. *Hydrogeology Journal*, *13*, 37–46.

Brunner, P., & Simmons, C. T. (2011). HydroGeoSphere: A fully integrated, physically based hydrological model. *Ground Water*, *50*(2), 170–176.

Brunner, P., Therrien, R., Renard, P., Simmons, C. T., & Hendricks Franssen, H.-J. (2017). Advances in understanding river-groundwater interactions. *Reviews of Geophysics*, *55*, 818–854. https://doi.org/10.1002/2017RG000556

Carniato, L., Schoups, G., van de Giesen, N., Seuntjens, P., Bastiaens, L., & Sapion, H. (2015). Highly parameterized inversion of groundwater reactive transport for a complex field site. *Journal of Contaminant Hydrology*, *173*, 38–58.

Cecil, L. D., & Green, J. R. (2000). Radon-222. In P. G. Cook & A. L. Herczeg (Eds.), *Environmental tracers in subsurface hydrology*. New York, NY: Springer.

Chow, R., Frind, M. E., Frind, E. O., Jones, J. P., Sousa, M. R., Rudolph, D. L., . . . Nowak, W. (2016). Delineating baseflow contribution areas for streams—A model and methods comparison. *Journal of Contaminant Hydrology*, *195*, 11–22.

Cook, P. G., & Böhlke, J.-K. (2000). Determining timescales for groundwater flow and solute transport. In P. G. Cook & A. L. Herczeg (Eds.), *Environmental tracers in subsurface hydrology*. New York, NY: Springer.

Cranswick, R. H., Cook, P. G., & Lamontagne, S. (2014). Hyporheic zone exchange fluxes and residence times inferred from riverbed temperature and radon data. *Journal of Hydrology*, *519*, 1870–1881.

Delottier, H., Pryet, A., & Dupuy, A. (2016). Why should practitioners be concerned about Predictive uncertainty of groundwater management models? *Water Resources Management*, *31*, 61–73.

Delsmann, J. R., Winters, P., Vandenbohede, A., Oude Essink, G. H. P., & Lebbe, L. (2016). Global sampling to assess the value of diverse observations in conditioning a real-world groundwater flow and transport model. *Water Resources Research*, *52*, 1652–1672. https://doi.org/10.1002/2014WR016476

Dirsch, H.-J. G. (2014). *FEFLOW—Finite element modeling of flow, mass and heat transport in porous and fractured media*. Heidelberg, Germany: Springer.
Doherty, J. E. (2015). *Calibration and uncertainty analysis for complex environmental models. PEST: Complete theory and what it means for modelling the real world*. Brisbane, Australia: Watermark Numerical Computing.
DURRIDGE. (2012). *RAD H2O user manual*. Billerica, MA: Author.
DURRIDGE. (2014). *RAD7 radon detector—User manual*. Billerica, MA: Author.
Fabryka-Martin, J. T. (1988). *Production of radionuclides in the earth and their hydrogeologic significance, with emphasis on chlorine-36 and iodine-129*. Tucson: University of Arizona.
Fetter, C. W. (2001). *Applied hydrogeology* (4th ed.). Upper Saddle Creek, NJ: Prentice Hall.
Feurer, D., Bailly, J.-S., Puech, C., Le Coarer, Y., & Viau, A. A. (2008). Very high-resolution mapping of river-immersed topography by remote sensing. *Progress in Physical Geography*, *32*(4), 403–419.
Figura, S., Livingstone, D. M., Hoehn, E., & Kipfer, R. (2011). Regime shift in groundwater temperature triggered by the Arctic Oscillation. *Geophysical Research Letters*, *38*, L23401. https://doi.org/10.1029/2011GL049749
Figura, S., Livingstone, D. M., & Kipfer, R. (2013). Competing controls on groundwater oxygen concentrations revealed in multidecadal time series from riverbank filtration sites. *Water Resources Research*, *49*, 7411–7426. https://doi.org/10.1002/2013WR013750
Figura, S., Livingstone, D. M., & Kipfer, R. (2015). Forecasting groundwater temperature with linear regression models using historical data. *Ground Water*, *53*(6), 943–954.
Fleckenstein, J. H., Niswonger, R. G., & Fogg, G. E. (2006). River-aquifer interactions, geologic heterogeneity, and low-flow management. *Ground Water*, *44*(6), 837–852.
Frei, S., Lischeid, G., & Fleckenstein, J. H. (2010). Effects of micro-topography on surface–subsurface exchange and runoff generation in a virtual riparian wetland—A modeling study. *Advances in Water Resources*, *33*(11), 1388–1401.
Gardner, W. P., Harrington, G. A., Solomon, D. K., & Cook, P. G. (2011). Using terrigenic ^{4}He to identify and quantify regional groundwater discharge to streams. *Water Resources Research*, *47*, W06523. https://doi.org/10.1029/2010WR010276
Gerber, C., Vaikmäe, R., Aeschbach, W., Babre, A., Jiang, W., Leuenberger, M., . . . Purtschert, R. (2017). Using ^{81}Kr and noble gases to characterize and date groundwater and brines in the Baltic Artesian Basin on the one-million-year timescale. *Geochimica et Cosmochimica Acta*, *205*, 187–210.
Gianni, G., Richon, J., Perrochet, P., Vogel, A., & Brunner, P. (2016). Rapid identification of transience in streambed conductance by inversion of floodwave responses. *Water Resources Research*, *52*, 2647–2658. https://doi.org/10.1002/2015WR017154
Guillon, S., Sun, Y., Purtschert, R., Raghoo, L., Pili, E., & Carrigan, C. R. (2016). Alteration of natural ^{37}Ar activity concentration in the subsurface by gas transport and water infiltration. *Journal of Environmental Radioactivity*, *155*, 89–96.
Harbaugh, A. W. (2005). MODFLOW-2005, The U.S. Geological Survey Modular Ground-Water Model—The ground-water flow process. In *U.S. Geological Survey techniques and methods* (Vol. 6-A16). Reston, VA: USGS.
Harrington, G. A., Walker, G. R., Love, A. J., & Narayan, K. A. (1999). A compartmental mixing-cell approach for the quantitative assessment of groundwater dynamics in the Otway Basin, South Australia. *Journal of Hydrology*, *214*, 49–63.
Harvey, J. W., & Gooseff, M. (2015). River corridor science: Hydrologic exchange and ecological consequences from bedforms to basins. *Water Resources Research*, *51*, 6893–6922. https://doi.org/10.1002/2015WR017617
Hendricks Franssen, H. J., Kaiser, H.-P., Kuhlmann, U., Bauser, G., Stauffer, F., Müller, R., & Kinzelbach, W. (2011). Operational real-time modeling with ensemble Kalman filter of variably saturated subsurface flow including stream-aquifer interaction and parameter updating. *Water Resources Research*, *47*, W02532. https://doi.org/10.1029/2010WR009480
Herczeg, A. L., & Edmunds, W. M. (2000). Inorganic ions as tracers. In P. G. Cook & A. L. Herczeg (Eds.), *Environmental tracers in subsurface hydrology*. New York, NY: Springer.
Hoehn, E., & von Gunten, H. R. (1989). Radon in groundwater: A tool to assess infiltration from surface waters to aquifers. *Water Resources Research*, *25*(8), 1795–1803.
Huggenberger, P., Hoehn, E., Beschta, R., & Woessner, W. (1998). Abiotic aspects of channels and floodplains in riparian ecology. *Freshwater Biology*, *40*, 407–425.
Hunt, R. J., Feinstein, D. T., Pint, C. D., & Anderson, M. P. (2006). The importance of diverse data types to calibrate a watershed model of the Trout Lake Basin, Northern Wisconsin, USA. *Journal of Hydrology*, *321*, 286–296.
Irvine, D. J., Brunner, P., Hendricks Franssen, H.-J., & Simmons, C. T. (2012). Heterogeneous or homogeneous? Implications of simplifying heterogeneous streambeds in models of losing streams. *Journal of Hydrology*, *424–425*, 16–23.
Johnson, C., Armstrong, H., Wilson, W. H., & Biegalski, S. R. (2015). Examination of radioargon production by cosmic neutron interactions. *Journal of Environmental Radioactivity*, *140*, 123–129.
Käser, D., Graf, T., Cochand, F., McLaren, R. G., Therrien, R., & Brunner, P. (2014). Channel representation in physically based models coupling groundwater and surface water: Pitfalls and how to avoid them. *Ground Water*, *52*(6), 827–836.
Käser, D., & Hunkeler, D. (2015). Contribution of alluvial groundwater to the outflow of mountainous catchments. *Water Resources Research*, *52*, 680–697. https://doi.org/10.1002/2014WR016730
Kipfer, R., Aeschbach-Hertig, W., Peeters, F., & Stute, M. (2002). Noble gases in lakes and ground waters. In D. Porcelli, C. Ballentine, & R. Wieler (Eds.), *Noble gases in geochemistry and cosmochemistry* (pp. 615–700). Washington, DC: Mineralogical Society of America and Geochemical Society.
Kollet, S., & Maxwell, R. (2006). Integrated surface-groundwater flow modeling: A free-surface overland flow boundary condition in a parallel groundwater flow model. *Advances in Water Resources*, *29*(7), 954–998.
Kropf, P., Schiller, E., Brunner, P., Schilling, O. S., Hunkeler, D., & Lapin, A. (2014). *Wireless mesh networks and cloud computing for real time environmental simulations*. Paper presented at 10th International Conference on Computing and Information Technology (IC2IT2014), Phuket, Thailand.
Kurtz, W., Hendricks Franssen, H.-J., Brunner, P., & Vereecken, H. (2013). Is high-resolution inverse characterization of heterogeneous river bed hydraulic conductivities needed and possible? *Hydrology and Earth System Sciences*, *17*, 3795–3813. https://doi.org/10.5194/hess-17-3795-2013
Kurtz, W., Lapin, A., Schilling, O. S., Tang, Q., Schiller, E., Braun, T., . . . Brunner, P. (2017). Integrating hydrological modelling, data assimilation and cloud computing for real-time management of water resources. *Environmental Modelling & Software*, *93*, 418–135.
Lamontagne, S., Taylor, A. R., Cook, P. G., Crosbie, R. S., Brownbill, R., Williams, R. M., & Brunner, P. (2014). Field assessment of surface water–groundwater connectivity in a semi-arid river basin (Murray–Darling, Australia). *Hydrological Processes*, *28*, 1561–1572.
Lapin, A., Schiller, E., Kropf, P., Schilling, O. S., Brunner, P., Jamakovic-Kapic, A., . . . Maffioletti, S. (2014). Real-time environmental monitoring for cloud-based hydrogeological modelling with HydroGeoSphere. Paper presented at High Performance Computing and Communications Conference (IEEE HPCC14), Paris, France.

Larocque, M., Cook, P. G., Haaken, K., & Simmons, C. T. (2009). Estimating flow using tracers and hydraulics in synthetic heterogeneous aquifers. *Ground Water*, *47*(6), 786–796.
Li, Q., Unger, A. J. A., Sudicky, E. A., Kassenaar, D., Wexler, E. J., & Shikaze, S. (2008). Simulating the multi-seasonal response of a large-scale watershed with a 3D physically-based hydrologic model. *Journal of Hydrology*, *357*, 317–336.
Loosli, H. H., Lehmann, B. E., & Smethie, W. M. (2000). Noble gas radioisotopes: ^{37}Ar, ^{85}Kr, ^{39}Ar, ^{81}Kr. In P. G. Cook & A. L. Herczeg (Eds.), *Environmental tracers in subsurface hydrology*. New York, NY: Springer.
Loosli, H. H., & Purtschert, R. (2005). Rare gases. In J. Gat, K. F. Froehlich, & P. K. Aggarwal (Eds.), *Isotopes in the water cycle: Past, present and future of a developing science* (pp. 91–95). Vienna, Austria: IAEA.
Lucas, L. L., & Unterweger, M. P. (2000). Comprehensive review and critical evaluation of the half-life of tritium. *Journal of Research of the National Institute of Standards and Technology*, *105*(4), 541–549.
Mattle, N., Kinzelbach, W., Beyerle, U., Huggenberger, P., & Loosli, H. H. (2001). Exploring an aquifer system by integrating hydraulic, hydrogeologic and environmental tracer data in a three-dimensional hydrodynamic transport model. *Journal of Hydrology*, *242*(3–4), 183–196.
Mayer, A., Sültenfuß, J., Travi, Y., Rebeix, R., Purtschert, R., Claude, C., . . . Conchetto, E. (2014). A multi-tracer study of groundwater origin and transit-time in the aquifers of the Venice region (Italy). *Applied Geochemistry*, *50*, 177–198.
McCallum, J. L., Cook, P. G., Brunner, P., & Berhane, D. (2010). Solute dynamics during bank storage flows and implications for chemical base flow separation. *Water Resources Research*, *46*, W07541. https://doi.org/10.1029/2009WR008539
McCallum, J. L., Cook, P. G., & Simmons, C. T. (2014a). Limitations of the use of environmental tracers to infer groundwater age. *Ground Water*, *53*, 56–70.
McCallum, J. L., Cook, P. G., Simmons, C. T., & Werner, A. D. (2014b). Bias of apparent tracer ages in heterogeneous environments. *Ground Water*, *52*(2), 239–250.
McLaren, R. G. (2011). *GridBuilder—A preprocessor for 2-D, triangular element, finite-element programs*. Waterloo, ON, Canada: Groundwater Simulations Group, University of Waterloo.
Partington, D., Brunner, P., Frei, S., Simmons, C. T., Werner, A. D., Therrien, R., . . . Fleckenstein, J. H. (2013). Interpreting streamflow generation mechanisms from integrated surface-subsurface flow models of a riparian wetland and catchment. *Water Resources Research*, *49*, 5501–5519. https://doi.org/10.1002/wrcr.20405
Partington, D., Brunner, P., Simmons, C. T., Therrien, R., Werner, A. D., Dandy, G. C., & Maier, H. R. (2011). A Hydraulic Mixing-Cell method to quantify the groundwater component of streamflow within spatially distributed fully integrated surface water–groundwater flow models. *Environmental Modelling & Software*, *26*, 886–898.
Partington, D., Brunner, P., Simmons, C. T., Werner, A. D., Therrien, R., Maier, H. R., & Dandy, G. C. (2012). Evaluation of outputs from automated baseflow separation methods against simulated baseflow from a physically based, surface water-groundwater flow model. *Journal of Hydrology*, *458–459*, 28–39.
Partington, D., Therrien, R., Simmons, C. T., & Brunner, P. (2017). Blueprint for a coupled model of sedimentology, hydrology, and hydrogeology in streambeds. *Reviews of Geophysics*, *55*, 287–309. https://doi.org/10.1002/2016RG000530
Purtschert, R. (2008). Timescales and tracers. In W. M. Edmunds & P. Shand (Eds.), *Natural groundwater quality* (pp. 91–108). Oxford, UK: Blackwell.
Purtschert, R., Yokochi, R., & Sturchio, N. C. (2013). ^{81}Kr dating of old groundwater. In S. Suckow, P. Aggarwal, & L. Araguas-Araguas (Eds.), *Isotope methods for dating old groundwater*. Vienna, Austria: IAEA.
Rao, B. K., & Hathaway, D. L. (1989). A three-dimensional mixing cell solute transport model and its applications. *Ground Water*, *27*(4), 509–516.
Riedmann, R. A. (2011). *Separation of argon from atmospheric air and measurements of 37Ar for CTBT purposes*. Bern, Switzerland: University of Bern.
Riedmann, R. A., & Purtschert, R. (2011). Natural ^{37}Ar concentrations in soil air: Implications for monitoring underground nuclear explosions. *Environmental Science & Technology*, *45*, 8656–8664.
Riedmann, R. A., & Purtschert, R. (2016). Separation of argon from environmental samples for Ar-37 and Ar-39 analyses, *Separation and Purification Technology*, *170*, 217–223.
Schilling, O. S., Doherty, J., Kinzelbach, W., Wang, H., Yang, P. N., & Brunner, P. (2014). Using tree ring data as a proxy for transpiration to reduce predictive uncertainty of a model simulating groundwater–surface water–vegetation interactions. *Journal of Hydrology*, *519*, 2258–2271.
Schilling, O. S., Irvine, D. J., Hendricks Franssen, H. J., & Brunner, P. (2017). Estimating the spatial extent of unsaturated zones in heterogeneous river-aquifer systems. *Water Resources Research.* https://doi.org/10.1002/2017WR020409.
Schlosser, P., Stute, M., Dörr, H., Sonntag, C., & Münnich, K. O. (1988). Tritium/^{3}He dating of shallow groundwater. *Earth and Planetary Science Letters*, *89*, 353–362.
Schnegg, P.-A. (2003). *A new field fluorometer for multi-tracer tests and turbidity measurement applied to hydrogeological problems*. Paper presented at 8th International congress of the Brazilian Geophysical Society, Sociedade Brasileira de Geofisica, Rio de Janeiro, Brazil.
Simmons, C. T., Hunt, R. J., & Cook, P. G. (2012). Using every tool in the toolbox. *Ground Water*, *50*(3), 323.
Solomon, D. K. (2000). ^{4}He in groundwater. In P. G. Cook & A. L. Herczeg (Eds.), *Environmental tracers in subsurface hydrology*. New York, NY: Springer.
Solomon, D. K., & Cook, P. G. (2000). ^{3}H and ^{3}He. In P. G. Cook & A. L. Herczeg (Eds.), *Environmental tracers in subsurface hydrology*. New York, NY: Springer.
Solomon, D. K., Genereux, D. P., Plummer, L. N., & Busenberg, E. (2010). Testing mixing models of old and young groundwater in a tropical lowland rain forest with environmental tracers. *Water Resources Research*, *46*, W04518. https://doi.org/10.1029/2009WR008341
Sophocleus, M. (2002). Interactions between groundwater and surface water: The state of the science. *Hydrogeology Journal*, *10*, 52–67.
Spreafico, M., & Weingartner, R. (2005). Hydrologie der Schweiz. In *Ausgewählte Aspekte und Resultate*. Bern, Switzerland: Bundesamt für Wasser und Geologie.
swisstopo. (2010). *Bundesamt für Landestopografie swisstopo - swissALTI3D - Das hoch aufgelöste Terrainmodell der Schweiz*. Bern, Switzerland: swisstopo.
Tang, Q., Kurtz, W., Schilling, O. S., Brunner, P., Vereecken, H., & Hendricks Franssen, H.-J. (2017). The influence of riverbed heterogeneity patterns on river-aquifer exchange fluxes under different connection regimes. *Journal of Hydrology*, *554*, 383–396.
Therrien, R., McLaren, R. G., Sudicky, E. A., & Panday, S. (2010). *HydroGeoSphere: A three-dimensional numerical model describing fully-integrated subsurface and surface flow and solute transport. Hydrogeosphere manual*. Waterloo, ON, Canada: Groundwater Simulations Group.
Townley, L. R. (2012). Calibration and sensitivity analysis. In B. Barnett et al. (Eds.), *Australian groundwater modelling guidelines* (pp. 57–78). Canberra, Australia: National Water Commission.

Turnadge, C., & Smerdon, B. D. (2014). A review of methods for modelling environmental tracers in groundwater: Advantages of tracer concentration simulation. *Journal of Hydrology*, *519*, 3674–3689.

Visser, A., Fourré, E., Barbecot, F., Aquilina, L., Labasque, T., Vergnaud, V., & Esser, B. K. (2014). Intercomparison of tritium and noble gases analyses, $^{3}H/^{3}He$ ages and derived parameters excess air and recharge temperature. *Applied Geochemistry*, *50*, 130–141.

Vogt, T., Hoehn, E., Schneider, P., Freund, A., Schirmer, M., & Cirpka, O. A. (2010). Fluctuations of electrical conductivity as a natural tracer for bank filtration in a losing stream. *Advances in Water Resources*, *33*, 1296–1308.

Winter, T. C., Harvey, J. W., Franke, O. L., & Alley, W. M. (1998). *Ground water and surface water: A single resource*. Denver, CO: U.S. Geological Survey.

Würsten, M. (1991). *GWB—Hydrogeologische Untersuchungen Aeschau: Schlussbericht*. Zürich, Switzerland: Geotechnisches Institut.